

Modeling urban pollutant transport at multi-resolutions: Impacts of turbulent mixing

Zining Yang¹, Qiuyan Du¹, Qike Yang¹, Chun Zhao^{1,2,3*}, Gudongze Li¹, Zihan Xia¹,
Mingyue Xu¹, Renmin Yuan¹, Yubin Li⁴, Kaihui Xia¹, Jun Gu¹, and Jiawang Feng¹

¹Deep Space Exploration Laboratory/School of Earth and Space Sciences/CMA-USTC Laboratory of Fengyun Remote Sensing/State Key Laboratory of Fire Science/Institute of Advanced Interdisciplinary Research on High-Performance Computing Systems and Software, University of Science and Technology of China, Hefei, China

²Laoshan Laboratory, Qingdao, China

³CAS Center for Excellence in Comparative Planetology, University of Science and Technology of China, Hefei, China.

⁴School of Atmospheric Physics, Nanjing University of Information Science and Technology, Nanjing, China

16

17

18

19

*Corresponding author: Chun Zhao (chunzhao@ustc.edu.cn)

Key Points:

1. Higher horizontal resolutions improve BC surface concentration predictions by enhancing PBL mixing and vertical wind flux, especially at night.

2. Small-scale eddies resolved at higher horizontal resolutions strengthen vertical fluxes, increasing BC atmospheric lifetime and column concentrations.

3. Detailed land use and terrain in high horizontal resolution models enhance PBL mixing, refining pollutant transport and urban air quality simulations.

29 **Abstract**

30 Air pollution in cities impacts public health and climate. Turbulent mixing is
31 crucial in pollutant formation and dissipation, yet current atmospheric models struggle
32 to accurately represent it. Turbulent mixing intensity varies with model resolution,
33 which has rarely been analyzed. To investigate turbulent mixing variations at multi-
34 resolutions and their implications for urban pollutant transport, we conducted
35 experiments using WRF-Chem at 25, 5, and 1 km resolutions. The simulated
36 meteorological fields and black carbon (BC) concentrations are compared with
37 observations. Differences in turbulent mixing across multi-resolutions are more
38 pronounced at night, resulting in noticeable variations in BC concentrations. BC surface
39 concentrations decrease as resolution increases from 25 km to 5 km and further to 1 km,
40 but are similar at 5 km and 1 km resolutions. Enhanced planetary boundary layer (PBL)
41 mixing coefficients and vertical wind flux at higher resolutions reduce BC surface
42 concentration overestimations. The 1 km resolution parameterized lower mixing
43 coefficients than 5 km but resolved more small-scale eddies, leading to similar near-
44 surface turbulent mixing at both resolutions, while the intensity at higher altitudes is
45 greater at 1 km. This caused BC to be transported higher and farther, increasing its
46 atmospheric lifetime and column concentrations. Variations in mixing coefficients are
47 partly attributed to differences in land use and terrain, with higher resolutions providing
48 more detailed information that enhances PBL mixing coefficients, while grid size
49 remains crucial in regions with more gradual terrain and land use changes. This study
50 interprets how turbulent mixing affects simulated urban pollutant diffusion at multi-
51 resolutions.

52

53

54

55

56

57 **1. Introduction**

58 Since the middle of the 19th century, rapid economic growth and urbanization have
59 caused severe regional haze and photochemical smog pollution (Li et al., 2015; Li et
60 al., 2019; Ma et al., 2019). A variety of air pollution episodes mainly occur in cities
61 (Chan and Yao, 2008). Exposure to atmospheric particulate matter is one of the major
62 threats to public health (Yin et al., 2017; Liu et al., 2019). Accurate pollutant estimation
63 is crucial for the realization of pollution prevention goals. Pollution processes are
64 affected by many different factors, such as pollution source emissions (Li et al., 2017a),
65 physical and chemical characteristics of aerosols (Riccobono et al., 2014; Zhao et al.,
66 2018), topographic effects (Zhang et al., 2018), and meteorological conditions (Ye et
67 al., 2016). Significantly, pollutant concentrations are mainly gathered within the
68 planetary boundary layer (PBL), and PBL mixing processes are associated with intricate
69 turbulent eddies (Stull, 1988), which significantly affect the horizontal transport and
70 vertical diffusion of pollutants (Wang et al., 2018; Du et al., 2020; Ren et al., 2020; Ren
71 et al., 2021), as well as the formation of new aerosol particles (Wu et al., 2021).

72 The mechanism of turbulent transport has been widely investigated. The vertical
73 diffusion of pollutants in urban areas is affected by the structure of the urban boundary
74 layer (UBL), and different structures may lead to uneven spatial distribution of
75 pollutants (Han et al., 2009; Zhao et al., 2013c). First, meteorological conditions play
76 dominant roles in turbulent mixing of air pollutants within the atmospheric boundary
77 layer (ABL) (Xu et al., 2015; Miao et al., 2019). Unstable meteorological conditions
78 enhance turbulence, promoting pollutant dispersion, while stable conditions suppress it,
79 leading to pollutants accumulation. Previous studies have indicated that constant
80 stagnant winds and increased water vapor density inhibit the vertical diffusion of
81 pollutants, resulting in explosive growth of pollutants (Zhang et al., 2015a; Zhang et al.,
82 2015b; Wei et al., 2018; Zhong et al., 2018). Under these stable conditions, the inherent
83 characteristics of the stable boundary layer (SBL), particularly turbulence intermittency
84 (Costa et al., 2011), affect the heavy urban haze events by altering surface-atmosphere
85 exchanges (Wei et al., 2018; Ren et al., 2019a; Ren et al., 2019b; Wei et al., 2020; Ren

86 et al., 2021; Zhang et al., 2022). Second, diurnal variations in turbulent mixing between
87 day and night significantly influence changes in pollutant concentrations (Li et al., 2018;
88 Liu et al., 2020). In the daytime convective boundary layer (CBL), pollutants can be
89 mixed uniformly in a thick layer due to the intense turbulent mixing (Sun et al., 2018).
90 While in the nighttime SBL, reduced mixing and dispersion result in the accumulation
91 of pollutants near the surface (Holmes et al., 2015). Severe urban haze pollution
92 formation is typically accompanied with the development of nocturnal SBL (Pierce et
93 al., 2019; Li et al., 2020; Zhang et al., 2020; Li et al., 2022). Moreover, pollutants in
94 the residual layer can be mixed downward to the surface with the development of the
95 ABL the next morning (Chen et al., 2009; Sun et al., 2013; Quan et al., 2020). Overall,
96 the impact of turbulent mixing on urban pollution is important and complex.

97 Numerical simulation is an important method for studying turbulent mixing.
98 However, there are still challenges associated with accurately representing turbulent
99 mixing in numerical models. Previous ~~research has~~ ~~researches have~~ indicated that
100 turbulent mixing in current atmospheric chemical models is insufficient to capture
101 stable atmospheric conditions, potentially leading to rapid increases in severe haze in
102 urban areas (Wang et al., 2018; Peng et al., 2018; Ren et al., 2019b; Du et al., 2020).
103 ~~Von Kuhlmann et al. (2003) identified insufficient upward transport of ozone and its~~
104 ~~precursors due to weak convection.~~ Some studies revealed that WRF-Chem simulations
105 underestimate turbulent exchange within stable nocturnal boundary layers, allowing
106 unrealistic accumulation of pollutants near the surface (Tuccella et al., 2012; Berger et
107 al., 2016). Additionally, PBL parameterization schemes in current models may not
108 accurately represent intricate turbulent mixing, particularly in complex terrains, urban
109 areas, or extreme weather conditions. ~~Researches has~~ ~~ve~~ revealed that different PBL
110 parameterization schemes employed in WRF-Chem tend to underestimate turbulent
111 mixing when compared to observations (Hong et al., 2006; Banks and Baldasano, 2016;
112 Kim, 2006). Turbulent mixing coefficients diagnosed in atmospheric models
113 characterize the intensity of turbulent mixing (Cuchiara et al., 2014). However, these
114 models frequently underestimate mixing coefficients during the nighttime. ~~Previous~~
115 ~~research~~ ~~Researchers have~~ ~~has~~ employed various approaches to address this limitation.

116 Du et al. (2020) demonstrated that increasing the lower limit of PBL mixing coefficients
117 during nighttime significantly reduced the modeling biases in simulated pollutant
118 concentrations. Jia and Zhang (2021) utilized the new modified turbulent diffusion
119 coefficient to represent the mixing process of pollutants separately and improved the
120 simulation results of pollutant concentrations. Jia et al. (2021) employed the revised
121 turbulent mixing coefficient of particles using high-resolution vertical flux data of
122 particles according to the mixing length theory, and improved the overestimation of
123 pollutant concentrations. In conclusion, current atmospheric models commonly face
124 several challenges in accurately simulating turbulent mixing.

125 The representation of turbulent mixing in models is influenced by various factors,
126 including grid resolution, topography, boundary layer parameterization, atmospheric
127 dynamics, and land-surface processes. Among these factors, model resolution can
128 significantly affect turbulent mixing processes in atmospheric simulations, with
129 simulated turbulent mixing varying substantially across different resolutions. Qian et al.
130 (2010) evaluated model performance at 3 km, 15 km, and 75 km resolutions, finding
131 that only simulations at 3 km resolution accurately captured multiple concentration
132 peaks in observational data, indicating that turbulent mixing may play a critical role in
133 simulating pollutant concentrations. Fountoukis et al. (2013) conducted model
134 simulations at three resolutions and demonstrated that higher resolution reduced the
135 bias for BC concentration by more than 30% in the Northeastern United States during
136 winter, attributing this improvement to better resolved pollutant dispersion. Tao et al.
137 (2020) found that changes in model resolution led to increased pollutant concentrations
138 in urban areas but decreased concentrations in west mountain regions, likely due to
139 differences in vertical and horizontal dispersion. In conclusion, previous researches
140 has~~s~~ve primarily focused on comparing pollutant concentrations across different model
141 resolutions, demonstrating that resolution significantly affects pollutant distribution
142 and dispersion. These studies suggest that turbulent mixing may play a crucial role.
143 However, few have systematically explored the specific mechanisms by which
144 turbulent mixing influences pollutant concentrations simulated at multi-resolutions,
145 despite their importance in determining urban atmospheric pollutions.

146 Motivated by aforementioned problems, this study aims to investigate differences
147 in pollutant concentrations across multi-resolutions and explore how the turbulent
148 mixing plays as a crucial role affecting pollutant concentrations at various resolutions.
149 Furthermore, we seek to determine whether higher-resolution simulations can address
150 the issue of inaccurate turbulent mixing in current models. The Weather Research and
151 Forecasting model coupled with Chemistry (WRF-Chem) is applied to simulate
152 pollutant and meteorological fields during the spring of 2019 in Hefei, a typical mega-
153 city and sub-center of the Yangtze River Delta (YRD) urban agglomeration in China,
154 with a population of nearly 10 million and an area of 11,445 km². Our study interprets
155 the various characteristics of black carbon (BC) distributions simulated at multi-
156 resolutions and focuses on the mechanisms involved. BC is selected as the primary
157 pollutant for this study due to its near-inert nature in the atmosphere and can be treated
158 as a representative tracer for turbulent mixing. The paper is organized as follows:
159 Section 2 introduces the WRF-Chem model configuration, the design of multi-
160 resolutions experiments, emissions from different sources, and observational data.
161 Section 3 evaluates model simulations across multi-resolutions against observations,
162 presents the spatial distributions of surface and column concentrations simulated at
163 three resolutions, and investigates the important turbulent mixing processes that
164 generate spatial variability in pollutant concentrations. Section 4 present the conclusion
165 and discussion of the analysis.

166

167 **2. Methodology**

168 **2.1 Models and Experiments**

169 **2.1.1 WRF-Chem**

170 The non-hydrostatic Weather Research and Forecasting (WRF) model includes
171 various options for dynamic cores and physical parameterizations that can be used to
172 simulate atmospheric processes over a wide range of spatial and temporal scales
173 (Skamarock et al., 2008). WRF-Chem, the chemistry version of the WRF model (Grell
174 et al., 2005), simulates trace gases and particulates interactively with the meteorological

175 fields. WRF-Chem treats photochemistry of trace gases and aerosol-related processes
176 with various different schemes (e.g. the Statewide Air Pollution Research Center
177 (SAPRC99) photochemical mechanism and the Model for Simulating Aerosol
178 Interactions and Chemistry (MOSAIC)).~~WRF-Chem contains some treatments for~~
179 ~~photochemistry and aerosols developed by the user community.~~ In this study, the
180 version of WRF-Chem updated by the University of Science and Technology of China
181 (USTC version of WRF-Chem) is used. Compared with the publicly released version,
182 this USTC version of WRF-Chem includes some additional functions such as the
183 diagnosis of radiative forcing of aerosol species, land surface coupled biogenic VOC
184 (volatile organic compound) emission, aerosol-snow interaction, improved PBL mixing
185 of aerosols and a detailed diagnosis of the contributions of each crucial process to
186 pollutant concentrations (Zhao et al., 2013a; Zhao et al., 2013b; Zhao et al., 2014; Zhao
187 et al., 2016; Hu et al., 2019; Du et al., 2020; Zhang et al., 2021).

188 The configuration of WRF-Chem in this study is given in Table 1. The ~~Statewide~~
189 ~~Air Pollution Research Center (SAPRC99)~~ photochemical mechanism (Carter, 2000) is
190 chosen to simulate the gas-phase chemistry, and the ~~Model for Simulating Aerosol~~
191 ~~Interactions and Chemistry (MOSAIC)~~ is ~~also~~ selected for aerosol processes (Zaveri
192 and Peters, 1999; Zaveri et al., 2008). The MOSAIC aerosol scheme includes important
193 physical and chemical processes such as nucleation, condensation, coagulation,
194 aqueous-phase chemistry, and water uptake by aerosols. Sulfate, nitrate, ammonium,
195 sea salt, mineral dust, organic matter (OM), BC, and other (unspecified) inorganics
196 (OIN) constitute the prognostic species in MOSAIC. The aerosol direct effect is
197 coupled to the Rapid Radiative Transfer Model (RRTMG) (Mlawer et al., 1997; Iacono
198 et al., 2000) for both SW (shortwave) and LW (longwave) radiation as implemented by
199 Zhao et al. (2011). We also turned on the aerosol indirect effect, which represents the
200 interactions between aerosols and clouds, including the first and second indirect effects,
201 activation/resuspension, wet scavenging, and aqueous chemistry (Gustafson et al., 2007;
202 Chapman et al., 2009). The photolysis rate is computed by the Fast-J radiation
203 parameterization (Wild et al., 2000). Our simulation includes the secondary organic
204 aerosol (SOA) mechanism, a crucial aerosol process that can substantially reduce

205 discrepancies between simulated results and observations.

206 Another type of option is meteorological physics, including the Yonsei University
207 (YSU) nonlocal PBL parameterization scheme (Hong et al., 2006), the Noah land-
208 surface model (Chen and Dudhia, 2001) for the surface layer process, the Morrison
209 two-moment scheme (Morrison et al., 2009) for cloud microphysics, and the Rapid
210 Radiative Transfer Model (RRTMG) for longwave and shortwave radiation. The 25 km
211 resolution simulation turns on the option of cumulus parameterization, which uses the
212 Kain-Fritsch cumulus and shallow convection scheme (Kain, 2004) to simulate sub-
213 grid scale clouds and precipitation. However, this option is turned off in the other two
214 higher resolution simulations because the fine-resolution is sufficient to resolve the
215 cloud forming processes.

216

217 2.1.2 Numerical experiments

218 The study period spans from March 5th to March 20th, 2019. Following previous
219 research (Gustafson et al., 2011), the first five days are considered as the model spin-
220 up time, while the remaining integration period is used for analysis. Consequently, only
221 the results from March 10th to March 20th, 2019, are used in the analysis of this study.
222 Three different resolutions and computational domains are employed in our study. The
223 outer domain, covering East, North, and South China, has 140 x 105 grid cells (107.1°-
224 127.9°E, 17.1°-44.9°N) with a horizontal resolution of 25 km. The middle domain,
225 encompassing the entire YRD region in East China, has 250 x 250 grid cells (111.82°-
226 121.78°E, 27.02°-36.98°N) with a resolution of 5 km. The inner domain, covering most
227 of the Hefei region, consists of 150 x 150 grid cells (116.604°-117.796°E, 31.204°-
228 32.396°N) at a horizontal resolution of 1 km. The center of inner domain is the city of
229 Hefei, a typical mega-city of East China. Hefei, the capital city of Anhui province, is
230 located in the mid-latitude zone with a humid subtropical monsoon climate and serves
231 as a representative case for this study. The regions are shown in Figure S1. To facilitate
232 the comparison of discrepancies among the three simulations at different resolutions,
233 we have selected the innermost region as the main scope of study for this research, as
234 shown in Figure 1a.

235 In this study, we derive terrain information from a high-resolution (~ 1 km) US
236 Geological Survey (USGS) topographic data and interpolate it onto the WRF grid.
237 Therefore, the three domains with different resolutions exhibit varying degrees of
238 terrain detail. The 1 km grid resolves the most intricate topographic features, followed
239 by the 5 km grid, while the 25 km grid captures the least spatial detail. These multi-
240 resolutions topographic representations potentially influence pollutant turbulent mixing
241 processes, which will be analyzed in this study. The land cover dataset is derived from
242 a 1 km horizontal resolution dataset for China (Zhang et al., 2021). The land use
243 categories follow the United States Geological Survey's (USGS) 24-category
244 classification, and the dataset is based on China's land cover conditions as of 2015. This
245 provides a more accurate representation of current land cover, particularly for eastern
246 China, which has experienced intensive urban expansion since the 2000s. Figure 1b
247 shows the land cover data at different resolutions, with detailed descriptions of the
248 legend and land cover classes provided in Table S1. This set of simulations is referred
249 to as the baseline experiment. With the exception of part of Section 3.2.3, all other
250 analyses in this study are based on the results of these baseline experiments. Moreover,
251 to explore the differences in turbulent mixing simulated at multi-resolutions under
252 consistent land use conditions, we conducted an additional set of sensitivity
253 experiments referred to as the sensitivity experiment. The sensitivity experiment was
254 identical to the baseline experiment, except it used the default USGS land use category
255 data in WRF. Notably, this default USGS data in WRF's geographical static database
256 represents Chinese land use patterns before the 2000s, as shown in Figure S2. This
257 default dataset reflects land use distribution prior to China's significant urbanization.
258 Consequently, the land use data types have minor variations and remained generally
259 consistent across all three resolutions in the sensitivity experiment.

260 On the other hand, the vertical configuration within the PBL is also crucial for
261 accurately modeling pollutant dispersion. To better resolve the PBL structure and
262 mixing processes, we implemented a finer vertical resolution within the PBL. Identical
263 vertical layer distributions are maintained across all three horizontal resolutions (25 km,
264 5 km, and 1 km), ensuring direct comparability of turbulent mixing across different

265 horizontal resolutions. A total of 50 terrain-following vertical eta-layers extending from
266 the surface to approximately 15 km were used in all three resolution simulations, with
267 30 layers distributed below 2 km above the ground to describe the atmospheric
268 boundary structure in detail. The vertical layer was strategically designed with 7 layers
269 below 200 meters (each approximately 20 meters in height), 3 layers between 200 and
270 300 meters (each about 30 meters in height), and 8 layers between 300 and 1000 meters
271 (each approximately 80 meters in height). This configuration comprehensively captures
272 mixed layer development and key turbulent processes (e.g., entrainment and surface
273 flux exchange) through layer densification, which is sufficient to capture PBL turbulent
274 mixing. Jiang et al. (2024) and Jiang and Hu (2023) have demonstrated that the number
275 of model vertical layers primarily influences vertical distribution, with more vertical
276 grid layers producing a more stable vertical structure under stable boundary conditions
277 that better resolves boundary layer turbulence.

278 In order to allow for a straightforward comparison of multi-resolutions simulations
279 and facilitate the identification of differences between the high- and low-resolution
280 simulations, the corner locations of the 1 km and 5 km resolution domains are aligned
281 with the corner locations of the 25 km grid cell. Each grid cell in the 25 km simulation
282 consists of a 5 x 5 set of cells from the 5 km simulation, and each grid cell in the 5 km
283 simulation comprises 5 x 5 cells from the 1 km simulation, as shown in Figure S3. Thus,
284 exactly 25 grids at 5 km resolution and 625 grids at 1 km resolution are embedded
285 within each 25 km grid cell.

286 To ensure similar boundary forcing across the three simulations, initial and
287 boundary conditions are handled differently for the 25 km, 5 km, and 1 km resolution
288 domains. For the 25 km resolution, meteorological initial and lateral boundary
289 conditions are obtained from the National Center for Environmental Prediction (NCEP)
290 final reanalysis (FNL) data with $1^\circ \times 1^\circ$ resolution and 6 h temporal resolution. Initial
291 and boundary conditions for the trace gases and aerosol species are provided by the
292 quasi-global WRF-Chem simulation with 360 x 145 grid cells (67.5°S - 77.5°N , 180°W -
293 180°E) at $1^\circ \times 1^\circ$ resolution. The initial and boundary conditions for the simulation at
294 5 km resolution are derived from the simulation at 25 km resolution. Similarly, the

295 initial and boundary conditions for the simulation at 1 km resolution are derived from
296 the simulation at 5 km resolution. In this way, since the forcing for the study area is
297 consistent across multi-resolutions, differences in simulation results among multi-
298 resolutions can be attributed to disparities in model resolutions.

299

300 **2.1.3 Emissions**

301 Anthropogenic emissions for the outer quasi-global simulation are derived from the
302 Hemispheric Transport of Air Pollution version-2 (HTAPv2) at $0.1^\circ \times 0.1^\circ$ horizontal
303 resolution and a monthly temporal resolution for 2010 (Janssens-Maenhout et al., 2015).
304 The Multi-resolution Emission Inventory for China (MEIC) at $0.25^\circ \times 0.25^\circ$ horizontal
305 resolution for 2019 (Li et al., 2017a; Li et al., 2017b) is used to replace emissions over
306 China within the simulation domain. Emission differences significantly contribute to
307 pollutant concentration variability across multi-resolutions. Qian et al. (2010) showed
308 that sub-grid variability of emissions can contribute up to 50% of the variability near
309 Mexico City. To eliminate the impact of inconsistent emissions on pollutant
310 concentrations simulated at multi-resolutions, we ensured emission consistency across
311 all three domains by interpolating emissions for all species from the 25 km resolution
312 domain to both the 5 km and 1 km resolution domains. This study primarily focuses on
313 BC. ~~—~~ The spatial distribution of BC emissions is shown in Figure 2. Figure S4
314 illustrates BC emissions at three different resolutions, demonstrating similar spatial
315 patterns across multi-resolutions. Biomass burning emissions are obtained from the Fire
316 Inventory from NCAR (FINN) at 1 km horizontal resolution and an hour temporal
317 resolution (Wiedinmyer et al., 2011). The diurnal variation of biomass burning
318 emissions follows the suggestions by WRAP (2005), with injection heights based on
319 Dentener et al. (2006) from the Aerosol Comparison between Observations and Models
320 (AeroCom) project. Biogenic emissions were calculated using the Model of Emissions
321 of Gases and Aerosols from Nature (MEGAN) v3.0 model (Guenther, 2007; Zhang et
322 al., 2021).

323

324 **2.2 Observational data**

325 2.2.1 Meteorological data

326 The meteorological data were obtained from the observation tower at the University
327 of Science and Technology of China (USTC) in Hefei, Anhui, China (117.27°E,
328 31.84°N), indicated by a solid black triangle in Figure 1a. The tower measures
329 temperature, relative humidity, wind speed, and wind direction at 2 m, 4.5 m, 8 m, 12.5
330 m and 18 m heights. This site represents a typical urban surface within the study area.
331 The tower was installed on the roof of a teaching building, with its top 17 m above the
332 canopy plane. It is equipped with three RM Young 03002 anemometers and three
333 HPM155A temperature and humidity sensors to measure the aforementioned
334 meteorological parameters (Yuan et al., 2016; Liu et al., 2017). This study focuses on
335 analyzing temperature, relative humidity, and wind speed.

336 Additionally, we employed meteorological data from automatic weather stations
337 (AWSs), which were established based on the operational standards issued by the China
338 Meteorological Administration (CMA, 2018). The hourly data underwent quality
339 control (QC) by local meteorological bureaus of Anhui, following World
340 Meteorological Organization guidelines (Estevez et al., 2011). The QC included checks
341 of consistency, such as internal, temporal-spatial, and climatic range validations. These
342 QC data were used to determine daily mean, minimum, and maximum meteorological
343 variables. The AWSs recorded various parameters, including air temperature (T, °C),
344 wind speed (U, m/s), air pressure (P, Pa), and wind direction. In this study, we focus on
345 the 3-hourly 2 m temperature and 10 m wind speed obtained from four AWS stations
346 located in the study region. The four AWS sites are marked by purple solid dots in
347 Figure S5.

348

349 2.2.2 Pollutants data

350 We ~~derived~~ used the hourly BC observations from the air quality monitoring site on
351 the campus of USTC during spring (March 10 to March 20, 2019). In this study, we
352 focus on analyzing BC observational data to compare with model output. BC was
353 observed using a Multi-angle Absorption Photometer (MAAP, Model-5012)
354 manufactured by Thermo Scientific. This instrument is located approximately 260 m

355 north of the USTC meteorological tower. It takes advantage of the strong visible light
356 absorption properties of BC aerosols. There is a linear relationship between the
357 attenuation of the beam after passing through the aerosol sample and the load of BC
358 aerosols on the fiber membrane. The BC concentration is derived by inverting this
359 relationship. A light scattering measurement is incorporated into the chamber to correct
360 for multiple scattering effects caused by particle accumulation on the filter tape. The
361 MAAP-5012 Black Carbon Meter collects atmospheric aerosols using glass fiber filter
362 membranes and observes them at a wavelength of 670 nm.

363 Although this study primarily focuses on the simulation of BC, we conducted a
364 comprehensive validation of other air pollutants to ensure the reliability of the
365 simulation results. However, after being initially obtained via a parameterized PBL
366 scheme, the mixing coefficients for gases are then clipped to empirically chosen
367 thresholds of $1 \text{ m}^2/\text{s}$ over rural regions and $2 \text{ m}^2/\text{s}$ over urban regions, with the
368 distinction between rural and urban regions made based on the local CO emission
369 strength. Thus, the boundary layer mixing coefficient for gases in the WRF-Chem
370 model is implicitly influenced by emission resolution rather than directly controlled by
371 model resolution. Consequently, the existing adjustment process for gas mixing
372 coefficients, which relies on CO emission strength, is unsuitable for studying the impact
373 of model resolution on the turbulent mixing of gaseous pollutants. In contrast, the
374 mixing coefficients ~~of for~~ particulate matter ~~is are~~ directly calculated through boundary
375 layer parameterization without subsequent modifications. The publicly available
version of WRF-Chem defines a default lower limit of $0.1 \text{ m}^2/\text{s}$ for particulate matter
mixing coefficients. We did not implement the adjustment proposed by Du et al. (2020),
which suggest raising the lower limit of PBL mixing coefficient from $0.1 \text{ m}^2/\text{s}$ to $5 \text{ m}^2/\text{s}$
within the PBL. Although setting specific thresholds can improve simulation results,
such thresholds are predominantly empirical in nature, whether based on CO and PM_{2.5}
emissions or the $5 \text{ m}^2/\text{s}$ threshold suggested by Du et al. (2020). These threshold
adjustments effectively compensate for missing physical processes in the model by
artificially enhancing mixing intensity. Our approach focuses on understanding the
physical mechanisms responsible for the model's underestimation of nighttime mixing

385 intensity, with particular emphasis on how model resolution affects turbulent mixing
386 processes. Rather than employing empirical thresholds to align model output with
387 observations, we aim to investigate the fundamental causes of the discrepancies. We
388 contend that threshold approaches rely heavily on empirical data, lack sufficient
389 theoretical foundation, and may impede comprehensive understanding of the
390 underlying physical processes. Consequently, this study utilizes the default particulate
391 matter turbulent mixing coefficients in the model for our analyses. Thus, i
392 In this study, we limited our additional validation to PM_{2.5} (fine particulate matter with aerodynamic
393 diameters less than 2.5 μm), ~~whose-as its~~ mixing processes are governed by the same
394 resolution-dependent mechanisms as BC. Ground observations of hourly PM_{2.5} surface
395 concentrations during March 2019 were obtained from the website of the Ministry of
396 Environmental Protection of China (MEP of China). As our study concentrates on the
397 Hefei region, we selected 10 monitoring stations within this area for detailed analysis.
398 These stations are marked as black triangles in Figure S5.

399 While hourly observations for both meteorology and pollutants are available, model
400 outputs are provided at 3-hour intervals to balance computational efficiency and storage
401 requirements. Hourly output data would provide higher time resolution but significantly
402 increase storage demands. Given that we ran simulations at multi-resolutions (25 km,
403 5 km, and 1 km), hourly outputs would have generated prohibitively large data volumes.
404 On the other hand, this 3-hour output interval remains sufficient for our primary
405 research objective of analyzing daily pollutant variations (particularly BC) rather than
406 precise hourly comparisons. ~~We believe-t~~This approach effectively captures daily
407 variability patterns without losing essential detail. For direct comparisons, hourly
408 observations were sampled to match our 3-hour model output intervals.

409

410 **3. Results**

411 **3.1 Simulated meteorological fields at various horizontal resolutions**

412 Meteorological fields may play a crucial role in the turbulent mixing and pollutant
413 transport. In this study, we evaluate time series of simulated temperature, wind speed,

414 and relative humidity across three resolutions against observational data to assess
415 resolution impacts on these key meteorological variables. Figure 3a compares the time
416 series of observed and simulated 8-m wind speeds at the USTC site (117.27°E,
417 31.84°N). Simulation results among multi-resolutions are similar, attributing to
418 relatively flat and uncomplicated topography. The temporal trends of the simulations
419 closely align with observational data, exhibiting distinct diurnal variations
420 characterized by higher values during the daytime and lower values at night.
421 Additionally, the model struggles to capture some moments accurately, overestimating
422 wind speed when it suddenly increases. For instance, on March 20 at noon, while the
423 observed peak wind speed is approximately 6 m/s, simulations at 25 km and 5 km
424 resolutions produced maximum wind speeds of approximately 9 m/s, significantly
425 exceeding the observed value, with only the 1 km resolution simulation yielding results
426 close to the observation. Figure 3b compares the 2-m temperature simulated at three
427 different resolutions with the observation. The multi-resolutions simulation results
428 exhibit remarkable consistency and closely align with observations. Temperature
429 displays a pronounced diurnal variation, fluctuating between 5 and 30 °C with relative
430 stability. However, the model occasionally underestimates or overestimates values at
431 certain time points. As shown in Figure 3c, the multi-resolutions simulated results
432 demonstrate consistency and accurately capture the diurnal variation trend of observed
433 relative humidity (RH). Model results are highly consistent with observations, both
434 reaching a maximum of 100%.

435 Additionally, Figure S6 displays the time series of observed and simulated
436 meteorological variables averaged across four AWS stations in the study region. Figure
437 S6a presents a comparison of 10-m wind speed simulated at three different resolutions,
438 revealing generally consistent results with observations. The overall pattern is similar
439 to that observed at the single USTC station, characterized by a clear diurnal variation
440 with higher wind speeds during daytime and lower speeds at night. However,
441 simulations at all three resolutions occasionally deviate from observations. For example,
442 on March 11, the 5 km and 1 km resolution models overestimate wind speed at
443 approximately 7 m/s compared to the observed 4 m/s. Conversely, on March 14 during

444 the daytime, all three resolutions underestimate wind speed, simulating around 2 m/s
445 against an observed value of 4 m/s. Figure S6b compares the simulated 2-m
446 temperatures across three resolutions with observational data. The simulated
447 temperatures are remarkably similar across all resolutions and show strong correlation
448 with observations throughout most of the study period. Only a few outliers were noted,
449 which minimally impact the overall pattern. For example, all resolution models
450 overestimate temperature at noon on March 20, simulating approximately 28°C while
451 the observed temperature is only about 20°C.

452 In summary, the simulated meteorological variables across multi-resolutions
453 demonstrate strong similarity and closely match the observations, with only occasional
454 minor discrepancies. However, our subsequent analysis reveals that the variations in
455 pollutant concentrations across multi-resolutions cannot be attributed to the minor
456 discrepancies observed in the time series of meteorological variables.

457

458 **3.2 Simulated BC surface concentrations and impacts of turbulent mixing at 459 various horizontal resolutions**

460 3.2.1 Surface concentrations simulated at three different horizontal resolutions

461 The spatial distribution of BC surface concentrations across multi-resolutions in the
462 study area is illustrated in Figure 4. As the resolution improves from 25 km to 5 km and
463 further to 1 km, BC surface concentrations reveal more detailed spatial features. Figure
464 4a presents the simulation results across multi-resolutions, averaged over the whole day.
465 Significant variations exist from coarse resolutions to fine resolutions, with surface
466 concentrations decreasing as resolution increases from 25 km to 5 km and further to 1
467 km. BC surface concentrations range from 0 to 9 $\mu\text{g}/\text{m}^3$. At 25 km resolution, there is a
468 notable discrepancy between the spatial distributions of BC concentrations and
469 emissions (Fig. 2). The highest simulated concentration at 25 km resolution is located
470 west of the USTC site, while maximum emissions are centered at the USTC site. Our
471 analysis indicates that the difference in turbulent mixing between these two regions
472 leads to spatial inconsistency between BC surface concentrations and emissions. The
473 details of this phenomenon will be discussed in section 3.2.2. Figure 4b illustrates the

474 spatial distribution of BC surface concentrations during the daytime. The differences in
475 surface concentrations among multi-resolutions are minimal, with values falling within
476 the range of 0 to 5 $\mu\text{g}/\text{m}^3$. In the central urban areas, the BC surface concentration
477 simulated at 25 km resolution is marginally lower than those simulated at finer
478 resolutions. Moreover, during the daytime, simulated BC concentrations over Chaohu
479 lake areas are notably higher than in other regions, potentially due to the impact of dry
480 deposition velocity. Figure S7 shows the spatial distribution of dry deposition velocity,
481 revealing lower values over lakes compared to other areas. This lower dry deposition
482 velocity leads to higher pollutant concentrations over lakes compared to land areas after
483 pollutants transport to the lake surface during the daytime. At night, dry deposition
484 velocity is similar to that of surrounding non-urban land areas. Consequently, nighttime
485 BC concentrations over lakes are approximately equal to those in surrounding areas.
486 Figure 4c demonstrates the spatial distribution of BC surface concentrations during
487 nighttime. Compared to daytime, BC surface concentrations are notably higher in all
488 major urban regions at night, with high-resolution simulations capturing more spatial
489 variations. In conclusion, BC surface concentrations decrease as resolution increases
490 from 25 km to 5 km and further 1 km. However, the spatial distribution of BC surface
491 concentrations at 5 km and 1 km resolutions are similar throughout the whole day.

492 To facilitate a more accurate and direct comparison of results across multi-
493 resolutions, we refine coarse grids to match fine grids. The detailed refinement process
494 is described in Text S1. Figure S8a exhibits the spatial differences in BC surface
495 concentrations between 25 km and 5 km resolutions, as well as between 25 km and 1
496 km resolutions, averaged over the whole day. It reveals that coarse-resolution (25 km
497 resolution) simulations generally yield higher BC surface concentrations than fine-
498 resolutions (5 km and 1 km resolution) simulations across most areas. The largest
499 disparities mainly occur in central urban areas with complex underlying surfaces and
500 complicated flow patterns. Figure S8b demonstrates the spatial differences in BC
501 surface concentrations between 25 km and 5 km resolutions, as well as between 25 km
502 and 1 km resolutions during the daytime, revealing smaller disparities mostly ranging
503 between -1 and 1 $\mu\text{g}/\text{m}^3$. In contrast, Figure S8c depicts pronounced differences in BC

504 concentrations between 25 km and 5 km resolutions, as well as between 25 km and 1
505 km resolutions during the nighttime, with most areas exhibiting disparities exceeding 2
506 $\mu\text{g}/\text{m}^3$. The largest differences are mainly concentrated in urban areas. These findings
507 indicate that diversities in BC surface concentrations among multi-resolutions are
508 primarily attributable to nocturnal concentrations in urban areas. However, differences
509 between 5 km and 1 km resolutions are small compared to those between 25 km and
510 finer resolutions (5 km and 1 km). BC surface concentrations are approximately equal
511 in the 5 km and 1 km simulations, as shown in Figure S9.

512 Furthermore, BC observations from the USTC monitoring station were utilized to
513 validate the simulated BC surface concentrations. Figure 5 illustrates the diurnal
514 variation of BC surface concentrations averaged over the USTC site. Both observations
515 and simulations exhibit a pronounced diurnal variation, with lower concentrations
516 during the daytime and higher concentrations at night. During the daytime, BC surface
517 concentrations simulated at three resolutions are comparable to the observational data.
518 However, nighttime simulations significantly overestimate BC surface concentrations.
519 As resolution increases from 25 km to 5 km and 1 km, the simulated surface
520 concentrations decrease, aligning more closely with observations. The 25 km resolution
521 simulations yield the highest concentrations, with a maximum value of approximately
522 $12 \mu\text{g}/\text{m}^3$, nearly double the observed values. In contrast, BC surface concentrations
523 simulated at 5 km and 1 km resolutions are similar and more closely align with
524 nocturnal observations, peaking at around $9 \mu\text{g}/\text{m}^3$. In conclusion, the diurnal variation
525 of the observation is better captured by high-resolution (5 km and 1 km) simulations.
526 The performance of BC surface concentrations across multi-resolutions demonstrates
527 that coarse grid spacing inadequately captures local pollutant distributions.

528 To verify the accuracy and comprehensiveness of the simulation results, we further
529 analyzed the diurnal variation of $\text{PM}_{2.5}$ surface concentrations. Figure S10 illustrates
530 the diurnal variation of simulated $\text{PM}_{2.5}$ surface concentrations across multi-resolutions
531 compared with observations. The diurnal pattern of $\text{PM}_{2.5}$ closely resembles that of BC,
532 characterized by higher concentrations at night and lower concentrations during
533 daytime. Across all resolutions, the model slightly underestimates daytime $\text{PM}_{2.5}$

534 surface observations while overestimating nighttime values. Notably, increased
535 horizontal resolution substantially improves nocturnal simulations. The 25 km
536 resolution simulation generates an anomalous midnight peak ($105 \mu\text{g}/\text{m}^3$), resulting in
537 a +61% bias, whereas the 5 km and 1 km resolutions substantially mitigate these
538 deviations to approximately 30%. To further examine the contribution of each $\text{PM}_{2.5}$
539 component to the diurnal variation across multi-resolutions, Figure S11 shows the
540 diurnal variations of four $\text{PM}_{2.5}$ constituents (sulfate (SO_4^{2-}), nitrate (NO_3^-), OIN, and
541 organic carbon (OC)) averaged over 10 MEP sites in Hefei. Significant differences
542 emerge in the diurnal variations of these components across multi-resolution
543 simulations. Specifically, the surface concentrations of NO_3^- , OIN, and OC exhibit a
544 consistent diurnal pattern, with lower concentrations during daytime and higher
545 concentrations at night. As resolution increases from 25 km to 5 km and 1 km, the
546 simulated components surface concentrations decrease, aligning more closely with
547 observations.

548 The total concentration of $\text{PM}_{2.5}$ and its components demonstrates significant
549 sensitivity to horizontal resolutions. Coarse resolution simulations underestimate
550 turbulent mixing capacity, resulting in overestimated concentrations. Higher resolution
551 simulations more accurately capture vertical mixing within the PBL. For secondary
552 particles such as sulfates and nitrates, formation rates depend heavily on local precursor
553 substance concentrations (SO_2 , NO_x). Higher resolution simulations may enable more
554 realistic representation of precursor substance diffusion, leading to reduced local
555 concentration gradients and consequently slower secondary aerosol formation rates.
556 Additionally, variations in $\text{PM}_{2.5}$ surface concentrations across multi-resolutions may
557 also stem from complex secondary particle generation mechanisms. For instance,
558 liquid-phase oxidation of sulfates in clouds is sensitive to local cloud water distribution,
559 with higher resolutions better capturing small-scale cloud structures that potentially
560 alter sulfate formation efficiency. The formation of ammonium nitrate (NH_4NO_3) is
561 particularly sensitive to temperature and humidity variations. At higher resolutions,
562 temperature and humidity gradients induced by urban heat island effects or
563 topographical variations can be more realistically simulated, influencing the

564 distribution of gaseous nitric acid (HNO_3) and particulate nitrate (NO_3^-). Dry deposition
565 processes may also contribute to resolution-dependent variations, as local differences
566 in surface roughness (including buildings and vegetation) become more apparent at
567 higher resolutions, directly affecting particulate deposition velocity rates. Overall, the
568 simulation results for major air pollutants fall within a reasonable error range compared
569 to observational data, confirming the reliability of the model for this study.

570 We now aim to further investigate the underlying factors contributing to the
571 discrepancies in atmospheric pollutant simulations, with a particular focus on BC,
572 across different spatial resolutions. Previous studies have indicated that the diurnal
573 variation of atmospheric particulate matter concentrations is primarily controlled by
574 daily variations of PBL mixing and pollutants emissions (Du et al., 2020). The diurnal
575 variation of BC emissions peak during the daytime and are lower at night. During
576 nighttime, pollutants are trapped within the shallow boundary layer due to the reduced
577 turbulent mixing, resulting in elevated surface concentrations of atmospheric
578 particulate matter. As the boundary layer develops in the morning, pollutants rapidly
579 diffuse and are transported to upper atmospheric layers, leading to relatively low
580 surface concentrations. Therefore, the turbulent mixing process plays a crucial role in
581 determining pollutant concentrations.

582

583 3.2.2 Impacts of turbulent mixing on BC surface concentrations at three different
584 horizontal resolutions

585 To investigate the vertical mixing depth influencing pollutant diffusion, we first
586 analyze the PBL height, as illustrated in Figure 6. Figure 6a shows the spatial
587 distribution of the PBL height simulated at three different resolutions, averaged over
588 the whole day. Higher-resolution simulations yield lower PBL heights and capture more
589 intricate details compared to lower-resolution simulations. This trend is consistent
590 during both daytime and nighttime. Figure 6b demonstrates that the PBL height exceeds
591 0.9 km across most regions during the daytime. Notably, due to strong topographic
592 influences, the PBL height in the vicinity of Chaohu Lake is remarkably low, typically
593 less than 0.1 km. Conversely, in the southwestern region, characterized by higher

594 elevations and more complex terrain, the PBL height surpasses 1.1 km. Figure 6c
595 depicts the nighttime PBL heights at three different resolutions. These heights
596 predominantly fall below 0.3 km, significantly lower than those during the daytime.
597 The PBL height gradually decreases as the resolution increases, which should typically
598 lead to higher BC surface concentrations. However, BC surface concentrations actually
599 decrease as resolution increases from 25 km to 5 km and 1km (Figure 4). Consequently,
600 the PBL height alone cannot explain the differences in pollutant simulations among
601 multi-resolutions in this study.

602 Previous studies have established that PBL mixing coefficients are critical
603 determinants in air quality modeling (Du et al., 2020). In WRF-Chem, turbulent mixing
604 within the boundary layer is partially governed by PBL mixing coefficients generated
605 by the PBL parameterization scheme. It is worth noting that the mixing coefficients for
606 atmospheric particulate matter and gases are two distinct variables in the current version
607 of WRF-Chem. The boundary layer mixing coefficient for gases is initially obtained
608 via a parameterized PBL scheme but undergoes additional modification through an
609 empirical parameterization that enhances gas mixing based on CO emission strength
610 (Kuhn et al., 2024). This enhancement applies to gas pollutants when using the
611 MOSAIC aerosol scheme, as implemented in this study. Specifically, gas mixing
612 coefficients are clipped to empirically chosen thresholds of $1 \text{ m}^2/\text{s}$ over rural regions
613 and $2 \text{ m}^2/\text{s}$ over urban regions, with the distinction between rural and urban regions
614 made based on the local CO emission strength. In contrast, the mixing coefficient of
615 particulate matter is directly calculated through boundary layer parameterization
616 without subsequent modifications. Our study focuses exclusively on the turbulent
617 mixing of atmospheric particulate matter, analyzing the aerosol mixing coefficient with
618 the default lower limit of $0.1 \text{ m}^2/\text{s}$ as specified in the publicly released version of WRF-
619 Chem. Additionally, we have not implemented the mixing coefficient adjustments
620 proposed by Du et al. (2020), which suggest raising the lower limit of PBL mixing
621 coefficient from $0.1 \text{ m}^2/\text{s}$ to $5 \text{ m}^2/\text{s}$ within the PBL. We contend that threshold
622 approaches are primarily based on empirical data and may impede comprehensive
623 understanding of the underlying physical processes. Unlike gas mixing coefficients, tIn

624 our study, particulate matter mixing coefficients are ~~the particulate matter mixing~~
625 ~~coefficient is~~ directly calculated through boundary layer parameterization without
626 adjustments based on ~~pollutant emission data, thus not being limited by emission~~
627 ~~resolution~~ empirical settings. This approach allows the model to more accurately
628 represent the natural turbulent mixing processes. Consequently, we can investigate the
629 turbulent mixing intensity of particulate matter across different horizontal resolutions
630 and examine the true impact of grid resolution on pollutant mixing.

631 The spatial distribution of aerosol turbulent mixing coefficients at the lowest model
632 layer is analyzed, as shown in Figure 7. Figure 7a illustrates the simulation results
633 across multi-resolutions averaged over the whole day. The variations in PBL mixing
634 coefficients across different resolutions are evident, with high-resolution simulations
635 capturing more spatial characteristics. The spatial distribution of the PBL mixing
636 coefficient demonstrates strong correlation with land use type and terrain height, which
637 will be explored subsequently. Turbulent mixing coefficients range from 0 to 8 m²/s,
638 with peak values predominantly located in urban areas. Notably, the mixing coefficient
639 simulated at 25 km resolution near surface around USTC substantially exceeds that of
640 the western area, resulting in lower BC surface concentrations simulated at 25 km
641 resolution at USTC compared to its western regions (Figure 4). This discrepancy leads
642 to a mismatch between the spatial distribution of pollutant concentrations and emissions,
643 as discussed in section 3.2.1. During the daytime, the PBL mixing coefficients
644 simulated at three resolutions are relatively high, ranging from 0 to 17 m²/s, as shown
645 in Figure 7b. BC masses simulated across multi-resolutions are fully mixed within the
646 boundary layer, resulting in similar BC surface concentrations across these resolutions.
647 Conversely, turbulent mixing coefficients diminish considerably during the nighttime,
648 with maximum values approximately 3 m²/s, as shown in Figure 7c. The turbulent
649 mixing coefficient emerges as one of the important factors controlling surface pollutant
650 concentrations under stable nocturnal PBL conditions. Nighttime PBL coefficients are
651 higher at 5 km and 1 km resolutions compared to 25 km resolution across most of the
652 study area, resulting in lower BC surface concentrations at these two higher resolutions
653 during the nighttime. Figure S12 further illustrates the disparities in parametrized PBL

654 mixing coefficients between 25 km resolution and the two higher-resolution simulations.
655 However, Figure S13 shows that the ~~intension of~~ turbulent mixing coefficient
656 parameterized at 5 km resolution is larger than that at 1 km resolution, which fails to
657 explain the similar surface concentrations in these two higher-resolution (5 km and 1
658 km) simulations. To further investigate this phenomenon, we selected a meridional
659 section passing through the USTC site to analyze the distribution of vertical wind speed
660 flux, which represents the turbulent mixing directly resolved by large-scale dynamic
661 processes.

662 Figure 8 displays the cross section of meridional wind speed flux along the USTC
663 site simulated at three different resolutions. The upward vertical wind speed flux
664 simulated at 25 km resolution are near the surface. However, the 5 km resolution
665 simulation generates stronger upward motion at a slightly higher altitude, specifically
666 between 850 and 1000 hPa. Notably, the 1 km resolution simulation captures the highest
667 vertical wind speed flux, with relatively intensive upward motion extending beyond
668 500 hPa. The 1 km resolution can resolve small-scale eddies and capture the most
669 pronounced vertical wind speed fluxes. In comparison, simulations at 5 km resolution
670 are able to capture smaller-scale eddies, while those at 25 km resolution occasionally
671 capture larger-scale eddies. Despite the larger PBL mixing coefficients at 5 km
672 resolution compared to 1 km resolution near the surface, the upward vertical wind speed
673 flux at 1 km resolution reaches higher altitudes, indicating the presence of more small-
674 scale eddies and resulting in enhanced vertical turbulent mixing. Consequently, near the
675 surface, the combined effects of turbulent mixing, which is represented by both the
676 parameterized PBL mixing coefficient and the directly resolved vertical wind speed
677 flux, lead to similar BC surface concentrations at higher resolutions (5 km and 1 km)
678 simulations. Furthermore, Figure S14 shows the meridional cross section during
679 daytime and nighttime. During the day, the mixing height ~~vertically upward~~ is relatively
680 high at all three resolutions, allowing pollutants to be fully mixed and transported
681 within the PBL. This results in similar BC surface concentrations across multi-
682 resolutions. Conversely, at night, high-resolution simulations resolve more small-scale
683 eddies, resulting in vertical transport reaching higher altitudes and intensifying

684 turbulent mixing. In conclusion, pollutants in lower-resolutions (25 km) simulations
685 tend to accumulate near the surface, whereas at higher resolutions (5 km and 1 km)
686 simulations, pollutants are transported to higher heights. This phenomenon contributes
687 to imparities in BC surface concentration across multi-resolutions.

688

689 3.2.3 Impacts of land use type and terrain height on turbulent mixing coefficients at
690 three different horizontal resolutions

691 Previous analysis indicate that the PBL mixing coefficient is one of the main factors
692 contributing to the disparities in BC surface concentrations across multi-resolutions.
693 Therefore, we further explored the factors influencing the spatial distribution of the
694 PBL mixing coefficient. Our analysis reveals that the spatial distribution of the PBL
695 mixing coefficient is closely related to land use types and terrain height. Specifically,
696 the overall distribution of the turbulent mixing coefficient is closely resembled by the
697 land use types (Figure 1b and Figure 7). However, in areas with obvious magnitude
698 changes, such as east of the USTC site, the turbulent mixing coefficient displays distinct
699 gradient changes that are not reflected in land use patterns. Notably, the spatial
700 distribution of the topographic height (Figure 1a) in this region exhibits distinct gradient
701 changes similar to those of the turbulent mixing coefficients. Consequently, the spatial
702 distribution of the turbulent mixing coefficient is influenced by both terrain and land
703 use types. This correlation can be attributed to the inter-relationship among turbulent
704 mixing, friction velocity, terrain, and land use types. Terrain and land use types
705 influence friction velocity by modifying surface roughness, which in turn directly
706 affects turbulent mixing coefficients within the PBL. Higher surface roughness
707 typically lead to greater fiction velocity, subsequently enhancing turbulent intensity and
708 increasing the vertical mixing efficiency of pollutants within the PBL. To further
709 investigate this relationship, the spatial distribution of friction velocity is analyzed, as
710 shown in Figure 9. The analysis reveals that friction velocity increases as resolution
711 increases from 25 km to 5 km and 1 km resolutions, with finer resolutions (5 km and 1
712 km) capturing more spatial details. Differences in friction velocity are illustrated in
713 Figure S15. The spatial distribution of friction velocity indeed correlates with terrain

714 and land use patterns, consequently influencing the distribution of the PBL mixing
715 coefficient. As a result, the spatial distribution of the PBL mixing coefficient correlates
716 with land use types and terrain height.

717 Our study indicates that variations in land use type distribution simulated at
718 different horizontal resolutions are a significant factor causing changes in PBL mixing
719 coefficients across multi-resolutions. These variations in mixing coefficients relate
720 closely to BC surface concentrations, explaining specific patterns of BC surface
721 concentration distributions. For example, the BC surface concentration south of the
722 USTC site increases as resolution improves from 25 km to 5 km and 1 km resolutions
723 (Figure 4 and Figure S8), contrasting with concentration variations simulated in other
724 regions. Our analysis reveals that the turbulent mixing coefficient simulated at 25 km
725 resolution is higher compared to the two higher-resolution simulations in this area
726 (Figure 7 and Figure S12). Moreover, the spatial distribution of land use types indicates
727 that the 25 km resolution simulation resolves only a single urban land use type in this
728 area (Figure 1b). In contrast, higher resolution simulations capture additional land use
729 types beyond the urban, including lakes, farmland, and shrubs (Figure 1b). The
730 inclusion of these diverse land use types in the higher resolution leads to smaller PBL
731 mixing coefficients in this area, as the surface roughness associated with lakes,
732 farmland, and shrubs is generally lower than that of urban areas. As a result, the reduced
733 vertical mixing in the finer resolution (5 km and 1 km) simulations results in higher BC
734 surface concentrations south of the USTC site.

735 Additionally, to explore the differences in PBL mixing coefficients across multi-
736 resolutions under uniform land use conditions, we designed another set of sensitivity
737 experiments across three resolutions. As mentioned earlier, the only difference from the
738 baseline experiment was the use of the default USGS land use classification data in the
739 WRF model. As shown in Figure S2, land use type data at different horizontal
740 resolutions are approximately consistent in this setup. All other settings remained
741 identical to those in the baseline experiment.

742 Figure 10 presents the spatial distribution of PBL mixing coefficients in the
743 sensitivity experiment. Figure 10a illustrates the results across multi-resolutions

744 averaged over the whole day. Similar to the baseline experiment, increasing resolution
745 resolves more spatial details. For example, in the area where the USTC site is located,
746 the PBL mixing coefficient in the 25 km resolution simulation of the sensitivity
747 experiment is approximately $4.3 \text{ m}^2/\text{s}$, significantly lower than the $8 \text{ m}^2/\text{s}$ observed in
748 the baseline experiment. This pattern is consistent across higher resolutions (5 km and
749 1 km). This finding aligns with the spatial distribution of land use types used in both
750 sets of experiments (Figure 1b and Figure S2). The decrease in mixing coefficients in
751 the sensitivity experiment stems from its land use data failing to resolve urban land
752 types in urban areas. Figures 10b and 10c show the PBL mixing coefficients of the
753 sensitivity experiment during daytime and nighttime, respectively. Consistent with the
754 baseline experiment, the turbulent mixing coefficients during the day are substantially
755 higher than at night. The PBL coefficients in the nighttime simulations are higher at 5
756 km and 1 km resolutions compared to the 25 km resolution.

757 Additionally, Figure S16 further illustrates the differences in the parameterized
758 PBL mixing coefficient between the 25 km resolution and the two higher-resolution
759 simulations under roughly uniform land use conditions. Figure S16c shows that in the
760 city center, the boundary layer mixing coefficient parameterized at 5 km and 1 km
761 resolutions is higher than at the 25 km resolution during nighttime. Since urban areas
762 are primarily flat, topographical differences between different resolutions in urban areas
763 are minimal, almost negligible. Furthermore, because the land use types in the
764 sensitivity experiment are approximately consistent across different resolutions, the
765 main factor responsible for resolution-related differences in the PBL mixing
766 coefficients in urban areas is the grid size. Notably, in areas with significant topographic
767 variations, such as suburban and rural regions, the difference in boundary layer mixing
768 coefficients between 25 km and 5 km/1 km resolutions in the sensitivity experiment
769 strongly correlates with the spatial distribution of topographic differences. This directly
770 demonstrates that topographic height is also a key determinant of boundary layer
771 mixing coefficient distribution. Qian et al. (2010) indicated that the terrain affects the
772 transport and mixing of aerosols and trace gases, as well as their concentrations across
773 multi-resolutions, through its impact on meteorological fields such as wind and the PBL

774 structure. These terrain-related effects are particularly significant in regions with more
775 variable topography. Additionally, Figure S17 shows that the turbulent mixing intensity
776 parameterized at 5 km resolution in the sensitivity experiment is greater than at 1 km
777 resolution. Further analysis of the latitude-pressure cross section of BC concentrations
778 and vertical wind speed flux, as shown in Figure S18, indicates that, similar to the
779 baseline experiment, the 1 km resolution of the sensitivity experiment resolves more
780 small-scale turbulent eddies, capturing more prominent vertical wind speed flux, thus
781 resulting in stronger turbulent mixing.

782 Through comprehensive analysis of both baseline and sensitivity experiments, we
783 found that within the resolution range of 25 km to 5 km and 1 km, the spatial distribution
784 accuracy of land use types plays a decisive role in parameterizing the PBL mixing
785 coefficient. Finer land use type information at higher resolutions directly alters the
786 spatial distribution of the boundary layer mixing coefficient, with urban surfaces
787 significantly increasing the parameterized PBL mixing coefficient. Therefore,
788 accurately representing land use types, particularly urban surfaces, is critical for
789 parameterizing the PBL mixing coefficient. On the other hand, in the sensitivity
790 experiment, complex terrain areas with significant elevation (such as suburban, rural,
791 and hilly regions) increase mixing coefficients by enhancing surface roughness,
792 whereas this effect is weaker in flat urban areas. Consequently, differences in PBL
793 mixing coefficients across multi-resolutions strongly correlate with terrain precision.
794 Higher resolutions can resolve finer terrain variations, affecting local turbulent mixing
795 (such as terrain-induced mechanical turbulence). This confirms the dominant role of
796 high-resolution terrain and land use information in PBL mixing coefficient
797 parameterization. Notably, in regions where land use types and terrain height remain
798 relatively flat and consistent across different horizontal resolutions in the sensitivity
799 experiments, increasing resolution still leads to enhanced boundary layer mixing
800 coefficients, highlighting the importance of grid size for parameterizing the boundary
801 layer mixing coefficient. In the resolution range from 5 km to 1 km, higher resolution
802 slightly reduces the parameterized boundary layer mixing coefficient. However, the 1
803 km resolution model resolves more small-scale turbulent eddies, resulting in stronger

804 turbulent mixing at night. In summary, for parameterization of boundary layer mixing
805 coefficients across multi-resolutions, high-resolution surface information is more
806 important in regions with significant changes in land use types and terrain height. Grid
807 size is also crucial in regions with more gradual changes, where higher-resolution grids
808 consistently enhance boundary layer mixing representation. Therefore, to improve PBL
809 mixing coefficient simulation, priority should be given to ensuring accuracy of land use
810 data (especially spatial representation of urban types), precise terrain representation in
811 complex regions, and appropriated grid resolution to enhance turbulent mixing
812 simulation.

813

814 **3.3 Simulated BC column concentrations and impacts of turbulent mixing at
815 various horizontal resolutions**

816 3.3.1 Simulated BC column concentrations at three different horizontal resolutions

817 It is generally accepted that the turbulent mixing process primarily affects
818 pollutant surface concentrations by mixing surface pollutants into higher layers,
819 without altering the column concentration. However, in this study, BC column
820 concentrations exhibit differences across multi-resolutions simulations. Therefore, we
821 further investigate the spatial distribution of BC column concentrations and the main
822 mechanisms behind these variations. Figure 11a illustrates the spatial distribution of
823 BC column concentrations simulated at three resolutions, averaged over the whole day.
824 The regional average values for the three resolutions are 2041, 2150, and 2223 $\mu\text{g}/\text{m}^2$,
825 respectively. The 5 km and 1 km resolution simulations yield larger BC column
826 concentrations compared to 25 km resolution simulations. The spatial distribution of
827 BC column concentrations simulated at 25 km resolution is highly consistent with the
828 BC emission distributions (Figure 2), showing high concentrations in central urban
829 areas exceeding 2500 $\mu\text{g}/\text{m}^2$, while regions distant from urban centers demonstrate
830 lower concentrations, generally below 2100 $\mu\text{g}/\text{m}^2$. The 5 km resolution simulation
831 results indicate peak column concentrations concentrated in urban areas and spread
832 around, with the southwestern area approaching 2250 $\mu\text{g}/\text{m}^2$. The 1 km resolution
833 simulation results yield the largest BC column concentrations and demonstrate the most

834 pronounced diffusion tendency, with most areas exceeding 2250 ug/m^2 . Figure 11b and
835 Figure 11c reveal lower BC column concentrations during the daytime compared to
836 those at night, with a more pronounced dispersion trend of column concentrations
837 simulated at night. Figure S19 depicts the differences in BC column concentrations
838 between 25 km and 5 km resolutions, as well as between 25 km and 1 km resolutions,
839 revealing that BC column concentrations in coarser resolutions are marginally lower
840 than those in finer resolutions (5 km and 1 km) in most of the study areas. On the other
841 hand, the BC column concentration simulated at 1 km resolution are larger than those
842 at 5 km resolution, as shown in Figure S20. In conclusion, BC column concentrations
843 increases with increased resolutions, accompanied by a more pronounced dispersion
844 tendency towards higher and farther areas.

845

846 3.3.2 Impacts of turbulent mixing on BC column concentrations at three different
847 horizontal resolutions

848 We further analyze the mechanisms underlying the differences in BC column
849 concentrations across multi-resolutions in urban areas. Figure 12a displays the vertical
850 profiles of BC concentrations averaged over the study area. The BC profiles at 25 km
851 resolution exhibit significant variability, generally decreasing from the surface to higher
852 altitudes. The near-surface BC concentration is approximately three times higher than
853 those at high altitudes, with surface concentrations reaching about 3 ug/m^3 . At an
854 altitude of 100 m, the concentration drops to 1 ug/m^3 , while above this elevation, the
855 BC concentration is less than 1 ug/m^3 . Substantial disparities exist among multi-
856 resolutions simulations in the vertical profiles of BC concentrations. Our analyses
857 above have shown that near the surface, the parameterized mixing coefficients and
858 directly resolved vertical wind speed flux are lower at 25 km resolution compared to 5
859 km and 1 km resolutions, reducing the vertical mixing of pollutants in 25 km resolution
860 simulations. Thus, BC concentrations at 25 km resolution are higher near the surface
861 and lower at higher altitudes compared to high-resolution (5 km and 1 km) simulations.
862 Moreover, the parameterized PBL mixing coefficient at 1 km resolution is lower than at
863 5 km resolution in the atmosphere, but the directly resolved upward vertical wind speed

864 flux by the model dynamic process reaches higher altitudes at 1 km resolution compared
865 to 5 km resolution. Thus, due to the combined effects of these two processes, the
866 intensity of turbulent mixing is similar between the 5 km and 1 km resolutions at near-
867 surface levels, whereas it is greater at 1 km resolution than at 5 km resolution at higher
868 altitudes. In numerical models, sub-grid scale (SGS) turbulent diffusion is typically
869 simulated by parameterization schemes. However, as model resolution increases, such
870 as achieving 1 km resolution, the turbulent mixing is increasingly resolved by ~~the~~
871 dynamical framework of the model. This advancement allows the model to capture
872 dynamic structures and small-scale turbulence more accurately, significantly enhancing
873 the strength of turbulent mixing. The ~~direct resolveresolution~~ of dynamic processes
874 reduces reliance on traditional parameterization schemes, thereby decreasing the PBL
875 mixing coefficient parameterized at finer resolutions. In conclusion, at higher altitudes,
876 the enhanced turbulent mixing efficiently facilitates more ground-emitted pollutants to
877 higher height as resolution increases. Thus, BC concentrations at 5 km and 1 km
878 resolution are similar near surface, with 1 km resolution yielding the largest
879 concentrations at higher altitudes.

880 To further investigate the BC column concentrations and their dispersion tendency
881 towards farther areas, we analyzed the vertical profile of wind speed at three resolutions
882 averaged over the study area, as shown in Figure 12b. The vertical profile of wind speed
883 is relatively consistent across the three resolutions. From the ground to higher altitudes,
884 the overall wind speed gradually increases, transitioning from low speeds near the
885 surface to higher speeds aloft. Near the ground, the simulated average wind speed is
886 approximately 1 m/s, increasing to 4 m/s at an altitude of 1 km, and reaching an average
887 of about 7 m/s at an altitude of 2 km. In the upper atmosphere, characterized by larger
888 wind speeds, pollutants mixed up from near-surface can be transported and dispersed
889 farther. As previously mentioned, BC simulated in higher-resolution simulations can be
890 transported to higher altitudes, thus dispersing over greater distances by stronger winds.
891 Therefore, as the resolution increases, the trend of diffusion towards farther regions in
892 the simulated BC column concentrations becomes more pronounced.

893 As previously discussed, higher-resolution simulations facilitate BC transport to

894 greater altitudes and further distances. This phenomenon extends its atmospheric
895 lifetime, consequently resulting in increased column concentrations. Bauer et al. (2013)
896 noted that turbulent mixing and convective transport processes play a critical role in
897 determining BC lifetimes. Figure 13 illustrates the spatial distribution of BC lifetime,
898 calculated by dividing the BC column concentration by the dry deposition flux. It
899 demonstrates that BC lifetime gradually lengthens as resolution increases. The average
900 lifetime of BC column concentrations in the study area is 344 h, 350 h, and 382 h for
901 25 km, 5 km, and 1 km resolutions, respectively. These results clearly demonstrate that
902 BC simulated at higher resolutions exhibits prolonged atmospheric residence times.
903 Consequently, the BC column concentration is higher in high-resolution simulations.

904

905 **4. Conclusion and Discussion**

906 Turbulent mixing plays a crucial role in urban pollutant transport by enhancing the
907 diffusion of atmospheric pollutants. Current atmospheric models often underestimate
908 turbulent exchange within stable nocturnal boundary layers, and the turbulent mixing
909 varies markedly across different model horizontal resolutions. However, few studies
910 have analyzed how turbulent mixing processes across multi-resolutions affect pollutant
911 concentrations in urban areas. Therefore, our goal is to elucidate the variations in
912 pollutant concentrations across multi-resolutions and investigate the influence of
913 turbulent mixing on pollutant concentrations at various resolutions.

914 We conducted a three-nested WRF-Chem simulation at 25 km, 5 km, and 1 km
915 resolutions in the Hefei area. BC surface concentrations decrease as resolution increases
916 from 25 km to 5 km and further to 1 km but are similar at 5 km and 1 km resolutions,
917 showing significant diurnal variations with higher concentrations at night and lower
918 during the daytime. The BC surface concentrations across multi-resolutions align well
919 with USTC site observations during daytime but are overestimated at night, with this
920 overestimation decreasing at higher-resolution (5 km and 1 km). Disparities in BC
921 surface concentrations between the two finer-resolution and the 25 km resolution
922 simulations are primarily attributable to nocturnal concentrations. In addition, the

923 diurnal variation of PM_{2.5} surface concentrations simulated at different resolutions
924 follows the same trend as the observed concentrations at the national monitoring sites,
925 with slight underestimation during daytime and overestimation at night. The PBL
926 mixing coefficient plays a crucial role in controlling surface particulate matter
927 concentrations at night. Larger nighttime PBL mixing coefficients and higher vertical
928 wind speed flux at 5 km and 1 km resolutions compared to 25 km resolution near the
929 surface result in lower BC surface concentrations. However, the PBL mixing coefficient
930 at 5 km is larger than at 1 km resolution. Moreover, the upward vertical wind speed flux
931 resolved at 1 km resolution reaches higher altitudes compared to 25 km and 5 km
932 resolutions, indicating more small-scale eddies and resulting in enhanced turbulent
933 mixing. Consequently, near the surface, the combined effects of parametrized PBL
934 mixing coefficient and the directly resolved vertical wind speed flux lead to similar BC
935 surface concentrations at 5 km and 1 km resolutions.

936 Further analysis reveals that the spatial distribution of PBL mixing coefficients is
937 influenced by both land use types and terrain heights. The turbulent mixing coefficient
938 correlates with the spatial distribution of land use types at smaller scales, with urban
939 underlying surfaces notably increasing the parameterized PBL mixing coefficient. The
940 mixing coefficient also strongly correlates with terrain heights at larger scales,
941 particularly in regions with complex topography and significant elevation differences,
942 where higher terrain substantially enhances mixing coefficients. This correlation can be
943 attributed to the interrelationship among turbulent mixing coefficients, friction velocity,
944 terrain, and land use types. The static database of terrain and land use types employed
945 as model input determines the surface roughness. Higher surface roughness typically
946 leads to greater friction velocity, subsequently increasing the PBL mixing coefficients.
947 Moreover, in regions where land use types and terrain height remain relatively flat and
948 consistent across multi-resolutions, increasing resolution still enhances boundary layer
949 mixing coefficients, highlighting the importance of grid size. Thus, both surface
950 information and grid resolution are crucial for accurately parameterizing PBL mixing
951 coefficients, with priority given to accurate land use data, precise terrain representation,
952 and higher grid resolution to improve turbulent mixing simulations.

953 In WRF-Chem, the mixing coefficients of chemical species are clipped to
954 empirically chosen thresholds of $1 \text{ m}^2/\text{s}$ over rural areas and $2 \text{ m}^2/\text{s}$ over urban areas to
955 prevent unrealistically low values. These thresholds are modified based on differences
956 in anthropogenic CO and primary PM_{2.5} emissions between rural and urban regions.
957 Importantly, this adjustment applies exclusively to gases and not to aerosols when the
958 MOSAIC or MADE/SORGAM aerosol schemes are used. This is because the
959 adjustment does not couple with the aerosol PBL mixing scheme in WRF-Chem,
960 although potential modifications could be made for compatibility with the MOSAIC or
961 MADE/SORGAM scheme. Thus, the boundary layer mixing coefficient for gases is
962 implicitly influenced by emission resolution rather than directly controlled by model
963 resolution. In this study, this treatment caused gas mixing coefficients to converge
964 across different horizontal resolutions, preventing us from accurately assessing the
965 impact of horizontal resolution on gas turbulent mixing. For aerosols, however, the
966 original PBL mixing coefficients are retained, which are directly parametrized from
967 boundary layer parameterization schemes. Therefore, our focus is mainly on particulate
968 matter in this analysis and we omitted this modification for gases.

969 The variations in turbulent mixing across multi-resolution simulations not only
970 affect the BC surface concentration but also lead to different BC column concentrations.
971 BC column concentrations increase with improved resolutions, accompanied by a more
972 pronounced diffusion tendency towards higher altitudes and distant regions.
973 Throughout the atmosphere, turbulent mixing intensifies with improved resolutions,
974 resulting in pollutants being transported to higher altitudes. Concurrently, wind speed
975 increases with altitude, facilitating the pollutants which are mixed to higher altitudes to
976 be spread farther. Consequently, BC simulated at higher resolution is transported to
977 greater altitudes and dispersed to farther regions, thus persisting in the atmosphere for
978 longer periods and leading to larger lifetimes. As a result, BC column concentrations
979 increase with finer resolutions.

980 This study highlights the importance of model horizontal resolution in simulating
981 the dispersion of atmospheric pollutants. We observed that the enhanced turbulent
982 mixing strength in high-resolution can more accurately reproduce the vertical and

983 horizontal distribution of pollutants, thus aligning the simulated pollutant surface
984 concentrations more closely with actual observations. In contrast, turbulent mixing in
985 low-resolution simulations, primarily depending on boundary layer parameterizations,
986 may not adequately capture the dynamics of turbulence, leading to discrepancies
987 between the simulated and actual distribution of pollutants, particularly during the night
988 with stable boundary condition. Future research should focus on improving PBL
989 parameterization schemes to enhance model performance at lower resolutions, thereby
990 better serving the needs of air pollution control and environmental management.

991 ~~Moreover, we~~ We have noted that the parameterized PBL mixing coefficient
992 decreases when transitioning from 5 km to 1 km resolution, alongside an increase in
993 vertical wind speed flux which represents turbulent mixing directly resolved by the
994 dynamical processes. This trend suggests that if the resolution was further increased to
995 LES scales, the parameterized PBL mixing coefficient might diminish significantly,
996 potentially approaching zero, while the turbulence mixing resolved directly by the
997 dynamics would intensify considerably. At LES scales, the majority of turbulent mixing
998 is directly resolved, capturing the atmospheric dynamical processes and turbulent
999 exchanges more realistically, thereby reducing the simulation biases caused by
1000 parameterization errors. This shift diminishes reliance on traditional boundary layer
1001 parameterizations to simulate turbulent mixing, leading to a substantial reduction in the
1002 parameterized boundary layer mixing coefficient. By capturing the finer details of
1003 atmospheric dynamics, the model provides a more realistic representation of turbulent
1004 mixing and related physical processes, which is crucial for understanding weather
1005 patterns, climate variability, and pollutant dispersion. However, due to the huge
1006 computational resources required for LES simulation, we have not yet performed an
1007 analysis at the LES scale, but it is worth further exploring in the future.

1008 Moreover, in addition to the influence of surface roughness on turbulence intensity,
1009 surface type significantly affects the CBL and turbulence mixing strength through
1010 differences in radiative flux absorption, reflection, and heat exchange. There are
1011 substantial variations in the absorption and reflection of shortwave radiation across
1012 different surface types. Urban areas typically have lower albedo, absorbing more

shortwave radiation, which increases surface temperature and transfers energy to the atmosphere as sensible heat. In contrast, vegetated areas generally have higher albedo and, through transpiration, release more latent heat while reducing sensible heat output. These differences in energy exchange between surface and atmosphere directly influence turbulence strength. Furthermore, the varying balance between sensible and latent heat fluxes across different surface types impacts turbulence intensity and CBL depth. For instance, urban areas, with stronger sensible heat flux, tend to generate more intense thermal convection, often resulting in a shallower CBL, while vegetated areas, with predominant latent heat flux, may develop more stable atmospheric conditions, potentially leading to a deeper CBL with weaker turbulence. These mechanisms of radiative absorption and heat exchange are crucial in the formation of the diurnal CBL and determining turbulence intensity. Future studies on land use impacts on turbulence mixing should therefore consider not only surface roughness but also radiative flux differences, sensible and latent heat exchange mechanisms, and the comprehensive effects of surface albedo on turbulence development.

Our analysis also found that higher-resolution facilitate transport over greater distances, suggesting that inter-city pollutant diffusion can be affected by model resolution, with coarse-resolution potentially reducing long-range transport and inter-urban impacts. While previous studies have examined pollutant formation mechanisms at specific resolutions and explored the physical and chemical interactions among megacities, few have considered the impacts of different resolutions on long-range transport between cities. Due to computational cost constraints, inter-urban impacts are not discussed in this study but deserve further investigation in the future. Finally, while vertical resolution is held constant in our study, we recognize that it could influence the interpretation of the turbulence processes in certain scenarios, especially in regions with complex vertical structures. Therefore, future work could systematically explore the interplay between vertical resolution and pollutant concentration or aerosol-boundary layer feedbacks.

1043
1044
1045
1046
1047
1048
1049
1050
1051 ***Data availability.*** The release version of WRF-Chem can be downloaded from
1052 http://www2.mmm.ucar.edu/wrf/users/download/get_source.html. The updated USTC
1053 version of WRF-Chem can be downloaded from <http://aemol.ustc.edu.cn/product/list/>
1054 or contact chunzhao@ustc.edu.cn. Additionally, code modifications will be
1055 incorporated into the release version of WRF-Chem in the future.

1056
1057 ***Author contributions.*** [Zining Yang](#) and [Chun Zhao](#) designed the experiments and
1058 conducted and analyzed the simulations. All authors contributed to the discussion and
1059 final version of the paper.

1060
1061 ***Competing interests.*** The contact author has declared that none of the authors has
1062 any competing interests.

1063 ***Acknowledgments.*** This research was supported by the National Key Research and
1064 Development Program of China (No. 2022YFC3700701), the Strategic Priority
1065 Research Program of Chinese Academy of Sciences (XDB0500303), National Natural
1066 Science Foundation of China (41775146), the USTC Research Funds of the Double
1067 First-Class Initiative (YD2080002007, KY2080000114), the Science and Technology
1068 Innovation Project of Laoshan Laboratory (LSKJ202300305), and the National Key
1069 Scientific and Technological Infrastructure project “Earth System Numerical
1070 Simulation Facility” (EarthLab). The study used the computing resources from the

1071 Supercomputing Center of the University of Science and Technology of China (USTC)
1072 and the Qingdao Supercomputing and Big Data Center.

1073 **Reference**

1074 Banks, R. F. and Baldasano, J. M.: Impact of WRF model PBL schemes on air quality
1075 simulations over Catalonia, Spain, *Science of the Total Environment*, 572, 98-113,
1076 <https://doi.org/10.1016/j.scitotenv.2016.07.167>, 2016.

1077 Bauer, S. E., Bausch, A., Nazarenko, L., Tsigaridis, K., Xu, B., Edwards, R., Bisiaux,
1078 M., and McConnell, J.: Historical and future black carbon deposition on the three
1079 ice caps: Ice core measurements and model simulations from 1850 to 2100, *Journal*
1080 *of Geophysical Research-Atmospheres*, 118, 7948-7961,
1081 <https://doi.org/10.1002/jgrd.50612>, 2013.

1082 Berger, A., Barbet, C., Leriche, M., Deguillaume, L., Mari, C., Chaumerliac, N., Begue,
1083 N., Tulet, P., Gazen, D., and Escobar, J.: Evaluation of Meso-NH and WRF-CHEM
1084 simulated gas and aerosol chemistry over Europe based on hourly observations,
1085 *Atmospheric Research*, 176, 43-63,
1086 <https://doi.org/10.1016/j.atmosres.2016.02.006>, 2016.

1087 Carter: Implementation of the SAPRC-99 chemical mechanism into the models-3
1088 framework, 2000.

1089 Chan, C. K. and Yao, X.: Air pollution in mega cities in China, *Atmospheric*
1090 *Environment*, 42, 1-42, <https://doi.org/10.1016/j.atmosenv.2007.09.003>, 2008.

1091 Chapman, E. G., Gustafson, W. I., Jr., Easter, R. C., Barnard, J. C., Ghan, S. J., Pekour,
1092 M. S., and Fast, J. D.: Coupling aerosol-cloud-radiative processes in the WRF-
1093 Chem model: Investigating the radiative impact of elevated point sources,
1094 *Atmospheric Chemistry and Physics*, 9, 945-964, <https://doi.org/10.5194/acp-9-945-2009>, 2009.

1096 Chen, F. and Dudhia, J.: Coupling an Advanced Land Surface–Hydrology Model with
1097 the Penn State–NCAR MM5 Modeling System. Part I: Model Implementation and
1098 Sensitivity, *Monthly Weather Review*, 129, 569-585, 2001.

1099 Chen, Y., Zhao, C., Zhang, Q., Deng, Z., Huang, M., and Ma, X.: Aircraft study of
1100 Mountain Chimney Effect of Beijing, China, *Journal of Geophysical Research-Atmospheres*, 114, <https://doi.org/10.1029/2008jd010610>, 2009.

1102 CMA, 2018: Technical Specifications for Maintenance of Regional Automatic Weather
1103 Stations. QX/T 465–2018. (in Chinese). Available at:
1104 <http://cmastd.cmatc.cn/standardView.jspx?id=3076>. Accessed on 5 May 2022.,
1105 2018.

1106 Costa, F. D., Acevedo, O. C., Mombach, J. C. M., and Degrazia, G. A.: A Simplified
1107 Model for Intermittent Turbulence in the Nocturnal Boundary Layer, Journal of the
1108 Atmospheric Sciences, 68, 1714-1729, <https://doi.org/10.1175/2011jas3655.1>,
1109 2011.

1110 Cuchiara, G. C., Li, X., Carvalho, J., and Rappenglueck, B.: Intercomparison of
1111 planetary boundary layer parameterization and its impacts on surface ozone
1112 concentration in the WRF-Chem model for a case study in Houston/Texas,
1113 Atmospheric Environment, 96, 175-185,
1114 <https://doi.org/10.1016/j.atmosenv.2014.07.013>, 2014.

1115 Dentener, F., Kinne, S., Bond, T., Boucher, O., Cofala, J., Generoso, S., Ginoux, P.,
1116 Gong, S., Hoelzemann, J. J., Ito, A., Marelli, L., Penner, J. E., Putaud, J. P., Textor,
1117 C., Schulz, M., van der Werf, G. R., and Wilson, J.: Emissions of primary aerosol
1118 and precursor gases in the years 2000 and 1750 prescribed data-sets for AeroCom,
1119 Atmospheric Chemistry and Physics, 6, 4321-4344, <https://doi.org/10.5194/acp-6-4321-2006>, 2006.

1120 Du, Q., Zhao, C., Zhang, M., Dong, X., Chen, Y., Liu, Z., Hu, Z., Zhang, Q., Li, Y.,
1121 Yuan, R., and Miao, S.: Modeling diurnal variation of surface PM_{2.5} concentrations
1122 over East China with WRF-Chem: impacts from boundary-layer mixing and
1123 anthropogenic emission, Atmospheric Chemistry and Physics, 20, 2839-2863,
1124 <https://doi.org/10.5194/acp-20-2839-2020>, 2020.

1125 Estevez, J., Gavilan, P., and Giraldez, J. V.: Guidelines on validation procedures for
1126 meteorological data from automatic weather stations, Journal of Hydrology, 402,
1127 144-154, <https://doi.org/10.1016/j.jhydrol.2011.02.031>, 2011.

1128 Fountoukis, C., Koraj, D., van der Gon, H. A. C. D., Charalampidis, P. E., Pilinis, C.,
1129 and Pandis, S. N.: Impact of grid resolution on the predicted fine PM by a regional
1130 3-D chemical transport model, Atmospheric Environment, 68, 24-32,

1132 <https://doi.org/10.1016/j.atmosenv.2012.11.008>, 2013.

1133 Grell, G. A., Peckham, S. E., Schmitz, R., McKeen, S. A., Frost, G., Skamarock, W. C.,
1134 and Eder, B.: Fully coupled "online" chemistry within the WRF model,
1135 Atmospheric Environment, 39, 6957-6975,
1136 <https://doi.org/10.1016/j.atmosenv.2005.04.027>, 2005.

1137 Guenther, A.: Estimates of global terrestrial isoprene emissions using MEGAN (Model
1138 of Emissions of Gases and Aerosols from Nature) (vol 6, pg 3181, 2006),
1139 Atmospheric Chemistry and Physics, 7, 4327-4327, <https://doi.org/10.5194/acp-7-4327-2007>, 2007.

1140 Gustafson, W. I., Jr., Qian, Y., and Fast, J. D.: Downscaling aerosols and the impact of
1141 neglected subgrid processes on direct aerosol radiative forcing for a representative
1142 global climate model grid spacing, Journal of Geophysical Research-Atmospheres,
1143 116, <https://doi.org/10.1029/2010jd015480>, 2011.

1144 Gustafson, W. I., Jr., Chapman, E. G., Ghan, S. J., Easter, R. C., and Fast, J. D.: Impact
1145 on modeled cloud characteristics due to simplified treatment of uniform cloud
1146 condensation nuclei during NEAQS 2004, Geophysical Research Letters, 34,
1147 <https://doi.org/10.1029/2007gl030021>, 2007.

1148 Han, S., Bian, H., Tie, X., Xie, Y., Sun, M., and Liu, A.: Impact of nocturnal planetary
1149 boundary layer on urban air pollutants: Measurements from a 250-m tower over
1150 Tianjin, China, Journal of Hazardous Materials, 162, 264-269,
1151 <https://doi.org/10.1016/j.jhazmat.2008.05.056>, 2009.

1152 Holmes, H. A., Sriramasamudram, J. K., Pardyjak, E. R., and Whiteman, C. D.:
1153 Turbulent Fluxes and Pollutant Mixing during Wintertime Air Pollution Episodes
1154 in Complex Terrain, Environmental Science & Technology, 49, 13206-13214,
1155 <https://doi.org/10.1021/acs.est.5b02616>, 2015.

1156 Hong, S.-Y., Noh, Y., and Dudhia, J.: A new vertical diffusion package with an explicit
1157 treatment of entrainment processes, Monthly Weather Review, 134, 2318-2341,
1158 <https://doi.org/10.1175/mwr3199.1>, 2006.

1159 Hu, Z., Huang, J., Zhao, C., Bi, J., Jin, Q., Qian, Y., Leung, L. R., Feng, T., Chen, S.,
1160 and Ma, J.: Modeling the contributions of Northern Hemisphere dust sources to
1161

1162 dust outflow from East Asia, Atmospheric Environment, 202, 234-243,
1163 <https://doi.org/10.1016/j.atmosenv.2019.01.022>, 2019.

1164 Iacono, M. J., Mlawer, E. J., Clough, S. A., and Morcrette, J. J.: Impact of an improved
1165 longwave radiation model, RRTM, on the energy budget and thermodynamic
1166 properties of the NCAR community climate model, CCM3, Journal of Geophysical
1167 Research-Atmospheres, 105, 14873-14890, <https://doi.org/10.1029/2000jd900091>,
1168 2000.

1169 Janssens-Maenhout, G., Crippa, M., Guizzardi, D., Dentener, F., Muntean, M., Pouliot,
1170 G., Keating, T., Zhang, Q., Kurokawa, J., Wankmueller, R., van der Gon, H. D.,
1171 Kuenen, J. J. P., Klimont, Z., Frost, G., Darras, S., Koffi, B., and Li, M.:
1172 HTAP_v2.2: a mosaic of regional and global emission grid maps for 2008 and 2010
1173 to study hemispheric transport of air pollution, Atmospheric Chemistry and
1174 Physics, 15, 11411-11432, <https://doi.org/10.5194/acp-15-11411-2015>, 2015.

1175 Jia, W. and Zhang, X.: Impact of modified turbulent diffusion of PM_{2.5} aerosol in WRF-
1176 Chem simulations in eastern China, Atmospheric Chemistry and Physics, 21,
1177 16827-16841, <https://doi.org/10.5194/acp-21-16827-2021>, 2021.

1178 Jia, W., Zhang, X., Zhang, H., and Ren, Y.: Application of Turbulent Diffusion Term of
1179 Aerosols in Mesoscale Model, Geophysical Research Letters, 48,
1180 <https://doi.org/10.1029/2021gl093199>, 2021.

1181 Jiang, L. and Hu, J.: Influence of the lowest model level height and vertical grid
1182 resolution on mesoscale meteorological modeling, Atmospheric Research, 296,
1183 <https://doi.org/10.1016/j.atmosres.2023.107066>, 2023.

1184 Jiang, L., Bessagnet, B., Meleux, F., Couvidat, F., Tognet, F., and Hu, J.: The role of
1185 vertical grid resolution and turbulent diffusion uncertainty on chemical transport
1186 modeling, Atmospheric Research, 312,
1187 <https://doi.org/10.1016/j.atmosres.2024.107759>, 2024.

1188 Kain, J. S.: The Kain-Fritsch convective parameterization: An update, Journal of
1189 Applied Meteorology, 43, 170-181, [https://doi.org/10.1175/1520-0450\(2004\)043<0170:Tkcpau>2.0.Co;2](https://doi.org/10.1175/1520-0450(2004)043<0170:Tkcpau>2.0.Co;2), 2004.

1191 Kim, S. W.: The Influence of PBL Parameterizations on the Distributions of Chemical

1192 Species in a Mesoscale Chemical Transport Model, WRF-Chem,

1193 Kuhn, L., Beirle, S., Kumar, V., Osipov, S., Pozzer, A., Boesch, T., Kumar, R., and

1194 Wagner, T.: On the influence of vertical mixing, boundary layer schemes, and

1195 temporal emission profiles on tropospheric NO₂ in WRF-Chem - comparisons to

1196 in situ, satellite, and MAX-DOAS observations, *Atmospheric Chemistry and*

1197 *Physics*, 24, 185-217, <https://doi.org/10.5194/acp-24-185-2024>, 2024.

1201 Li, H., Li, L., Huang, C., An, J., Yan, R., Huang, H., Wang, Y., Lu, Q., Wang, Q., Lou,

1202 S., Wang, H., Zhou, M., Tao, S., Qiao, L., and Chen, M.: Ozone Source

1203 Apportionment at Urban Area during a Typical Photochemical Pollution Episode

1204 in the Summer of 2013 in the Yangtze River Delta, *Environmental Science*, 36, 1-

1205 10, 2015.

1206 Li, L., An, J., Huang, L., Yan, R., Huang, C., and Yarwood, G.: Ozone source

1207 apportionment over the Yangtze River Delta region, China: Investigation of

1208 regional transport, sectoral contributions and seasonal differences, *Atmospheric*

1209 *Environment*, 202, 269-280, <https://doi.org/10.1016/j.atmosenv.2019.01.028>,

1210 2019.

1211 Li, M., Liu, H., Geng, G., Hong, C., Liu, F., Song, Y., Tong, D., Zheng, B., Cui, H.,

1212 Man, H., Zhang, Q., and He, K.: Anthropogenic emission inventories in China: a

1213 review, *National Science Review*, 4, 834-866, <https://doi.org/10.1093/nsr/nwx150>,

1214 2017a.

1215 Li, M., Zhang, Q., Kurokawa, J.-i., Woo, J.-H., He, K., Lu, Z., Ohara, T., Song, Y.,

1216 Streets, D. G., Carmichael, G. R., Cheng, Y., Hong, C., Huo, H., Jiang, X., Kang,

1217 S., Liu, F., Su, H., and Zheng, B.: MIX: a mosaic Asian anthropogenic emission

1218 inventory under the international collaboration framework of the MICS-Asia and

1219 HTAP, *Atmospheric Chemistry and Physics*, 17, 935-963,

1220 <https://doi.org/10.5194/acp-17-935-2017>, 2017b.

1221 Li, Q., Zhang, H., Jin, X., Cai, X., and Song, Y.: Mechanism of haze pollution in

1222 summer and its difference with winter in the North China Plain, *Science of the*

1223 *Total Environment*, 806, <https://doi.org/10.1016/j.scitotenv.2021.150625>, 2022.

1224 Li, Q., Wu, B., Liu, J., Zhang, H., Cai, X., and Song, Y.: Characteristics of the

1222 atmospheric boundary layer and its relation with PM_{2.5} during haze episodes in
1223 winter in the North China Plain, *Atmospheric Environment*, 223,
1224 <https://doi.org/10.1016/j.atmosenv.2020.117265>, 2020.

1225 Li, X.-B., Wang, D.-S., Lu, Q.-C., Peng, Z.-R., and Wang, Z.-Y.: Investigating vertical
1226 distribution patterns of lower tropospheric PM_{2.5} using unmanned
1227 aerial vehicle measurements, *Atmospheric Environment*, 173, 62-71,
1228 <https://doi.org/10.1016/j.atmosenv.2017.11.009>, 2018.

1229 Liu, C., Huang, J., Wang, Y., Tao, X., Hu, C., Deng, L., Xu, J., Xiao, H.-W., Luo, L.,
1230 Xiao, H.-Y., and Xiao, W.: Vertical distribution of PM_{2.5} and
1231 interactions with the atmospheric boundary layer during the development stage of
1232 a heavy haze pollution event, *Science of the Total Environment*, 704,
1233 <https://doi.org/10.1016/j.scitotenv.2019.135329>, 2020.

1234 Liu, C., Chen, R., Sera, F., Vicedo-Cabrera, A. M., Guo, Y., Tong, S., Coelho, M. S. Z.
1235 S., Saldiva, P. H. N., Lavigne, E., Matus, P., Ortega, N. V., Garcia, S. O., Pascal,
1236 M., Stafoggia, M., Scortichini, M., Hashizume, M., Honda, Y., Hurtado-Diaz, M.,
1237 Cruz, J., Nunes, B., Teixeira, J. P., Kim, H., Tobias, A., Iniguez, C., Forsberg, B.,
1238 Astrom, C., Ragettli, M. S., Guo, Y.-L., Chen, B.-Y., Bell, M. L., Wright, C. Y.,
1239 Scovronick, N., Garland, R. M., Milojevic, A., Kysely, J., Urban, A., Orru, H.,
1240 Indermitte, E., Jaakkola, J. J. K., Rytí, N. R. I., Katsouyanni, K., Analitis, A.,
1241 Zanobetti, A., Schwartz, J., Chen, J., Wu, T., Cohen, A., Gasparrini, A., and Kan,
1242 H.: Ambient Particulate Air Pollution and Daily Mortality in 652 Cities, *New
1243 England Journal of Medicine*, 381, 705-715,
1244 <https://doi.org/10.1056/NEJMoa1817364>, 2019.

1245 Liu, H., Yuan, R., Mei, J., Sun, J., Liu, Q., and Wang, Y.: Scale Properties of Anisotropic
1246 and Isotropic Turbulence in the Urban Surface Layer, *Boundary-Layer
1247 Meteorology*, 165, 277-294, <https://doi.org/10.1007/s10546-017-0272-z>, 2017.

1248 Ma, T., Duan, F., He, K., Qin, Y., Tong, D., Geng, G., Liu, X., Li, H., Yang, S., Ye, S.,
1249 Xu, B., Zhang, Q., and Ma, Y.: Air pollution characteristics and their relationship
1250 with emissions and meteorology in the Yangtze River Delta region during 2014-
2016, *Journal of Environmental Sciences*, 83, 8-20,

1252 <https://doi.org/10.1016/j.jes.2019.02.031>, 2019.

1253 Miao, Y., Li, J., Miao, S., Che, H., Wang, Y., Zhang, X., Zhu, R., and Liu, S.: Interaction
1254 Between Planetary Boundary Layer and PM_{2.5} Pollution in
1255 Megacities in China: a Review, Current Pollution Reports, 5, 261-271,
1256 <https://doi.org/10.1007/s40726-019-00124-5>, 2019.

1257 Mlawer, E. J., Taubman, S. J., Brown, P. D., Iacono, M. J., and Clough, S. A.: Radiative
1258 transfer for inhomogeneous atmospheres: RRTM, a validated correlated-k model
1259 for the longwave, Journal of Geophysical Research-Atmospheres, 102, 16663-
1260 16682, <https://doi.org/10.1029/97jd00237>, 1997.

1261 Morrison, H., Thompson, G., and Tatarki, V.: Impact of Cloud Microphysics on the
1262 Development of Trailing Stratiform Precipitation in a Simulated Squall Line:
1263 Comparison of One- and Two-Moment Schemes, Monthly Weather Review, 137,
1264 991-1007, <https://doi.org/10.1175/2008mwr2556.1>, 2009.

1265 Peng, Y., Wang, H., Li, Y., Liu, C., Zhao, T., Zhang, X., Gao, Z., Jiang, T., Che, H., and
1266 Zhang, M.: Evaluating the performance of two surface layer schemes for the
1267 momentum and heat exchange processes during severe haze pollution in Jing-Jin-
1268 Ji in eastern China, Atmospheric Chemistry and Physics, 18, 17421-17435,
1269 <https://doi.org/10.5194/acp-18-17421-2018>, 2018.

1270 Pierce, A. M., Loria-Salazar, S. M., Holmes, H. A., and Gustin, M. S.: Investigating
1271 horizontal and vertical pollution gradients in the atmosphere associated with an
1272 urban location in complex terrain, Reno, Nevada, USA, Atmospheric Environment,
1273 196, 103-117, <https://doi.org/10.1016/j.atmosenv.2018.09.063>, 2019.

1274 Qian, Y., Gustafson, W. I., Jr., and Fast, J. D.: An investigation of the sub-grid
1275 variability of trace gases and aerosols for global climate modeling, Atmospheric
1276 Chemistry and Physics, 10, 6917-6946, <https://doi.org/10.5194/acp-10-6917-2010>,
1277 2010.

1278 Quan, J., Dou, Y., Zhao, X., Liu, Q., Sun, Z., Pan, Y., Jia, X., Cheng, Z., Ma, P., Su, J.,
1279 Xin, J., and Liu, Y.: Regional atmospheric pollutant transport mechanisms over the
1280 North China Plain driven by topography and planetary boundary layer processes,
1281 Atmospheric Environment, 221, <https://doi.org/10.1016/j.atmosenv.2019.117098>,

1282 2020.

1283 Ren, Y., Zhang, H., Wei, W., Cai, X., and Song, Y.: Determining the fluctuation of PM_{2.5}
1284 mass concentration and its applicability to Monin-Obukhov similarity, *Science of*
1285 *the Total Environment*, 710, <https://doi.org/10.1016/j.scitotenv.2019.136398>, 2020.

1286 Ren, Y., Zhang, H., Wei, W., Cai, X., Song, Y., and Kang, L.: A study on atmospheric
1287 turbulence structure and intermittency during heavy haze pollution in the Beijing
1288 area, *Science China-Earth Sciences*, 62, 2058-2068,
1289 <https://doi.org/10.1007/s11430-019-9451-0>, 2019a.

1290 Ren, Y., Zhang, H., Wei, W., Wu, B., Cai, X., and Song, Y.: Effects of turbulence
1291 structure and urbanization on the heavy haze pollution process, *Atmospheric*
1292 *Chemistry and Physics*, 19, 1041-1057, <https://doi.org/10.5194/acp-19-1041-2019>,
1293 2019b.

1294 Ren, Y., Zhang, H., Zhang, X., Li, Q., Cai, X., Song, Y., Kang, L., and Zhu, T.: Temporal
1295 and spatial characteristics of turbulent transfer and diffusion coefficient of PM_{2.5},
1296 *Science of the Total Environment*, 782, 782,
1297 <https://doi.org/10.1016/j.scitotenv.2021.146804>, 2021.

1298 Riccobono, F., Schobesberger, S., Scott, C. E., Dommen, J., Ortega, I. K., Rondo, L.,
1299 Almeida, J., Amorim, A., Bianchi, F., Breitenlechner, M., David, A., Downard, A.,
1300 Dunne, E. M., Duplissy, J., Ehrhart, S., Flagan, R. C., Franchin, A., Hansel, A.,
1301 Junninen, H., Kajos, M., Keskinen, H., Kupc, A., Kuerten, A., Kvashin, A. N.,
1302 Laaksonen, A., Lehtipalo, K., Makhmutov, V., Mathot, S., Nieminen, T., Onnela,
1303 A., Petaja, T., Praplan, A. P., Santos, F. D., Schallhart, S., Seinfeld, J. H., Sipila,
1304 M., Spracklen, D. V., Stozhkov, Y., Stratmann, F., Tome, A., Tsagkogeorgas, G.,
1305 Vaattovaara, P., Viisanen, Y., Vrtala, A., Wagner, P. E., Weingartner, E., Wex, H.,
1306 Wimmer, D., Carslaw, K. S., Curtius, J., Donahue, N. M., Kirkby, J., Kulmala, M.,
1307 Worsnop, D. R., and Baltensperger, U.: Oxidation Products of Biogenic Emissions
1308 Contribute to Nucleation of Atmospheric Particles, *Science*, 344, 717-721,
1309 <https://doi.org/10.1126/science.1243527>, 2014.

1310 Skamarock, W. C., Klemp, J. B., Dudhia, J., Gill, D. O., and Powers, J. G.: A
1311 Description of the Advanced Research WRF Version 3, NCAR Technical Note

1312 NCAR/TN-475+STR. June 2008. Mesoscale and Microscale Meteorology
1313 Division. National Center for Atmospheric Research. Boulder, 475, 2008.

1314 Stull, R. B.: An Introduction to Boundary Layer Meteorology, An Introduction to
1315 Boundary Layer Meteorology1988.

1316 Sun, T., Che, H., Qi, B., Wang, Y., Dong, Y., Xia, X., Wang, H., Gui, K., Zheng, Y.,
1317 Zhao, H., Ma, Q., Du, R., and Zhang, X.: Aerosol optical characteristics and their
1318 vertical distributions under enhanced haze pollution events: effect of the regional
1319 transport of different aerosol types over eastern China, Atmospheric Chemistry and
1320 Physics, 18, 2949-2971, <https://doi.org/10.5194/acp-18-2949-2018>, 2018.

1321 Sun, Y., Song, T., Tang, G., and Wang, Y.: The vertical distribution of
1322 PM_{2.5} and boundary-layer structure during summer haze in Beijing,
1323 Atmospheric Environment, 74, 413-421,
1324 <https://doi.org/10.1016/j.atmosenv.2013.03.011>, 2013.

1325 Tao, H., Xing, J., Zhou, H., Pleim, J., Ran, L., Chang, X., Wang, S., Chen, F., Zheng,
1326 H., and Li, J.: Impacts of improved modeling resolution on the simulation of
1327 meteorology, air quality, and human exposure to PM_{2.5}, O₃ in Beijing, China,
1328 Journal of Cleaner Production, 243, <https://doi.org/10.1016/j.jclepro.2019.118574>,
1329 2020.

1330 Tuccella, P., Curci, G., Visconti, G., Bessagnet, B., Menut, L., and Park, R. J.: Modeling
1331 of gas and aerosol with WRF-Chem over Europe: Evaluation and sensitivity study,
1332 Journal of Geophysical Research-Atmospheres, 117,
1333 <https://doi.org/10.1029/2011jd016302>, 2012.

1334 Von Kuhlmann, R., Lawrence, M. G., Crutzen, P. J., and Rasch, P. J.: A model for
1335 studies of tropospheric ozone and nonmethane hydrocarbons: Model description
1336 and ozone results, Journal of Geophysical Research-Atmospheres, 108,
1337 <https://doi.org/10.1029/2002jd002893>, 2003.

1338 Wang, H., Peng, Y., Zhang, X., Liu, H., Zhang, M., Che, H., Cheng, Y., and Zheng, Y.:
1339 Contributions to the explosive growth of PM_{2.5} mass due to aerosol-radiation
1340 feedback and decrease in turbulent diffusion during a red alert heavy haze in
1341 Beijing-Tianjin-Hebei, China, Atmospheric Chemistry and Physics, 18, 17717-

1342 17733, <https://doi.org/10.5194/acp-18-17717-2018>, 2018.

1343 Wei, W., Zhang, H., Cai, X., Song, Y., Bian, Y., Xiao, K., and Zhang, H.: Influence of
1344 Intermittent Turbulence on Air Pollution and Its Dispersion in Winter 2016/2017
1345 over Beijing, China, Journal of Meteorological Research, 34, 176-188,
1346 <https://doi.org/10.1007/s13351-020-9128-4>, 2020.

1347 Wei, W., Zhang, H., Wu, B., Huang, Y., Cai, X., Song, Y., and Li, J.: Intermittent
1348 turbulence contributes to vertical dispersion of PM_{2.5} in the North China Plain:
1349 cases from Tianjin, Atmospheric Chemistry and Physics, 18, 12953-12967,
1350 <https://doi.org/10.5194/acp-18-12953-2018>, 2018.

1351 Wiedinmyer, C., Akagi, S. K., Yokelson, R. J., Emmons, L. K., Al-Saadi, J. A., Orlando,
1352 J. J., and Soja, A. J.: The Fire INventory from NCAR (FINN): a high resolution
1353 global model to estimate the emissions from open burning, Geoscientific Model
1354 Development, 4, 625-641, <https://doi.org/10.5194/gmd-4-625-2011>, 2011.

1355 Wild, O., Zhu, X., and Prather, M. J.: Fast-j: Accurate simulation of in- and below-
1356 cloud photolysis in tropospheric chemical models, Journal of Atmospheric
1357 Chemistry, 37, 245-282, <https://doi.org/10.1023/a:1006415919030>, 2000.

1358 WRAP – Western Regional Air Partnership: 2002 Fire Emission Inventory for the
1359 WRAP Region – Phase II, Project No.178-6, available at:
1360 <http://www.wrapair.org/forums/fejf/tasks/FEJFTask7PhaseII.html> (last access: 30
1361 September 2021), 2005.

1362 Wu, H., Li, Z., Li, H., Luo, K., Wang, Y., Yan, P., Hu, F., Zhang, F., Sun, Y., Shang, D.,
1363 Liang, C., Zhang, D., Wei, J., Wu, T., Jin, X., Fan, X., Cribb, M., Fischer, M. L.,
1364 Kulmala, M., and Petaja, T.: The impact of the atmospheric turbulence-
1365 development tendency on new particle formation: a common finding on three
1366 continents, National Science Review, 8, <https://doi.org/10.1093/nsr/nwaa157>,
1367 2021.

1368 Xu, J., Yan, F., Xie, Y., Wang, F., Wu, J., and Fu, Q.: Impact of meteorological
1369 conditions on a nine-day particulate matter pollution event observed in December
1370 2013, Shanghai, China, Particuology, 20, 69-79,
1371 <https://doi.org/10.1016/j.partic.2014.09.001>, 2015.

1372 Ye, X., Song, Y., Cai, X., and Zhang, H.: Study on the synoptic flow patterns and
1373 boundary layer process of the severe haze events over the North China Plain in
1374 January 2013, Atmospheric Environment, 124, 129-145,
1375 <https://doi.org/10.1016/j.atmosenv.2015.06.011>, 2016.

1376 Yin, P., Brauer, M., Cohen, A., Burnett, R. T., Liu, J., Liu, Y., Liang, R., Wang, W., Qi,
1377 J., Wang, L., and Zhou, M.: Long-term Fine Particulate Matter Exposure and
1378 Nonaccidental and Cause-specific Mortality in a Large National Cohort of Chinese
1379 Men, Environmental Health Perspectives, 125, <https://doi.org/10.1289/ehp1673>,
1380 2017.

1381 Yuan, R., Luo, T., Sun, J., Liu, H., Fu, Y., and Wang, Z.: A new method for estimating
1382 aerosol mass flux in the urban surface layer using LAS technology, Atmospheric
1383 Measurement Techniques, 9, 1925-1937, <https://doi.org/10.5194/amt-9-1925-2016>,
1384 2016.

1385 Zaveri, R. A. and Peters, L. K.: A new lumped structure photochemical mechanism for
1386 large-scale applications, Journal of Geophysical Research-Atmospheres, 104,
1387 30387-30415, <https://doi.org/10.1029/1999jd900876>, 1999.

1388 Zaveri, R. A., Easter, R. C., Fast, J. D., and Peters, L. K.: Model for Simulating Aerosol
1389 Interactions and Chemistry (MOSAIC), Journal of Geophysical Research-
1390 Atmospheres, 113, <https://doi.org/10.1029/2007jd008782>, 2008.

1391 Zhang, H., Zhang, X., Li, Q., Cai, X., Fan, S., Song, Y., Hu, F., Che, H., Quan, J., Kang,
1392 L., and Zhu, T.: Research progress on estimation of atmospheric boundary layer
1393 height, Acta Meteorologica Sinica, 78, 522-536, 2020.

1394 Zhang, L., Zhang, H., Li, Q., Cai, X., and Song, Y.: Vertical dispersion mechanism of
1395 long-range transported dust in Beijing: Effects of atmospheric turbulence,
1396 Atmospheric Research, 269, <https://doi.org/10.1016/j.atmosres.2022.106033>,
1397 2022.

1398 Zhang, L., Sun, J. Y., Shen, X. J., Zhang, Y. M., Che, H., Ma, Q. L., Zhang, Y. W.,
1399 Zhang, X. Y., and Ogren, J. A.: Observations of relative humidity effects on aerosol
1400 light scattering in the Yangtze River Delta of China, Atmospheric Chemistry and
1401 Physics, 15, 8439-8454, <https://doi.org/10.5194/acp-15-8439-2015>, 2015a.

1402 Zhang, M., Zhao, C., Yang, Y., Du, Q., Shen, Y., Lin, S., Gu, D., Su, W., and Liu, C.:
1403 Modeling sensitivities of BVOCs to different versions of MEGAN emission
1404 schemes in WRF-Chem (v3.6) and its impacts over eastern China, *Geoscientific
1405 Model Development*, 14, 6155-6175, <https://doi.org/10.5194/gmd-14-6155-2021>,
1406 2021.

1407 Zhang, R., Wang, G., Guo, S., Zarnora, M. L., Ying, Q., Lin, Y., Wang, W., Hu, M., and
1408 Wang, Y.: Formation of Urban Fine Particulate Matter, *Chemical Reviews*, 115,
1409 3803-3855, <https://doi.org/10.1021/acs.chemrev.5b00067>, 2015b.

1410 Zhang, Z., Xu, X., Qiao, L., Gong, D., Kim, S.-J., Wang, Y., and Mao, R.: Numerical
1411 simulations of the effects of regional topography on haze pollution in Beijing,
1412 *Scientific Reports*, 8, <https://doi.org/10.1038/s41598-018-23880-8>, 2018.

1413 Zhao, C., Liu, X., Leung, L. R., and Hagos, S.: Radiative impact of mineral dust on
1414 monsoon precipitation variability over West Africa, *Atmospheric Chemistry and
1415 Physics*, 11, 1879-1893, <https://doi.org/10.5194/acp-11-1879-2011>, 2011.

1416 Zhao, C., Leung, L. R., Easter, R., Hand, J., and Avise, J.: Characterization of speciated
1417 aerosol direct radiative forcing over California, *Journal of Geophysical Research-
1418 Atmospheres*, 118, 2372-2388, <https://doi.org/10.1029/2012jd018364>, 2013a.

1419 Zhao, C., Li, Y., Zhang, F., Sun, Y., and Wang, P.: Growth rates of fine aerosol particles
1420 at a site near Beijing in June 2013, *Advances in Atmospheric Sciences*, 35, 209-
1421 217, <https://doi.org/10.1007/s00376-017-7069-3>, 2018.

1422 Zhao, C., Chen, S., Leung, L. R., Qian, Y., Kok, J. F., Zaveri, R. A., and Huang, J.:
1423 Uncertainty in modeling dust mass balance and radiative forcing from size
1424 parameterization, *Atmospheric Chemistry and Physics*, 13, 10733-10753,
1425 <https://doi.org/10.5194/acp-13-10733-2013>, 2013b.

1426 Zhao, C., Hu, Z., Qian, Y., Leung, L. R., Huang, J., Huang, M., Jin, J., Flanner, M. G.,
1427 Zhang, R., Wang, H., Yan, H., Lu, Z., and Streets, D. G.: Simulating black carbon
1428 and dust and their radiative forcing in seasonal snow: a case study over North
1429 China with field campaign measurements, *Atmospheric Chemistry and Physics*, 14,
1430 11475-11491, <https://doi.org/10.5194/acp-14-11475-2014>, 2014.

1431 Zhao, C., Huang, M., Fast, J. D., Berg, L. K., Qian, Y., Guenther, A., Gu, D.,

1432 Shrivastava, M., Liu, Y., Walters, S., Pfister, G., Jin, J., Shilling, J. E., and Warneke,
1433 C.: Sensitivity of biogenic volatile organic compounds to land surface
1434 parameterizations and vegetation distributions in California, Geoscientific Model
1435 Development, 9, 1959-1976, <https://doi.org/10.5194/gmd-9-1959-2016>, 2016.

1436 Zhao, X. J., Zhao, P. S., Xu, J., Meng, W., Pu, W. W., Dong, F., He, D., and Shi, Q. F.:
1437 Analysis of a winter regional haze event and its formation mechanism in the North
1438 China Plain, Atmospheric Chemistry and Physics, 13, 5685-5696,
1439 <https://doi.org/10.5194/acp-13-5685-2013>, 2013c.

1440 Zhong, J., Zhang, X., Dong, Y., Wang, Y., Liu, C., Wang, J., Zhang, Y., and Che, H.:
1441 Feedback effects of boundary-layer meteorological factors on cumulative
1442 explosive growth of PM_{2.5} during winter heavy pollution episodes in Beijing from
1443 2013 to 2016, Atmospheric Chemistry and Physics, 18, 247-258,
1444 <https://doi.org/10.5194/acp-18-247-2018>, 2018.

1445

1446

1447

1448

1449

1450

1451

1452

1453

1454

1455

1456

1457

1458

1459

1460

1461

1462

1463

1464

1465

1466

1467

1468

1469

1470

Table 1 WRF-Chem model configuration

Horizontal resolution	25 km & 5 km & 1 km
Domain size	140 x 105 & 250 x 250 & 150 x 150
Simulation period	5 March to 21 March 2019
Gas-phase chemistry scheme	SAPRC99 mechanism
Radiation scheme	Fast-J
PBL scheme	YSU scheme
Microphysics scheme	Morrison two-moment scheme
Land surface scheme	Noah land-surface scheme
Cumulus scheme	Kain-Fritsch (25 km grid only)
Surface layer scheme	Revised MM5 Monin-Obukhov scheme
Longwave radiation scheme	RRTMG scheme
Shortwave radiation scheme	RRTMG scheme

1471

1472

1473

1474

1475

1476

1477

1478

1479

1480

1481

1482

1483

1484

1485

1486

1487

1488

1489

1490

1491

1492

1493

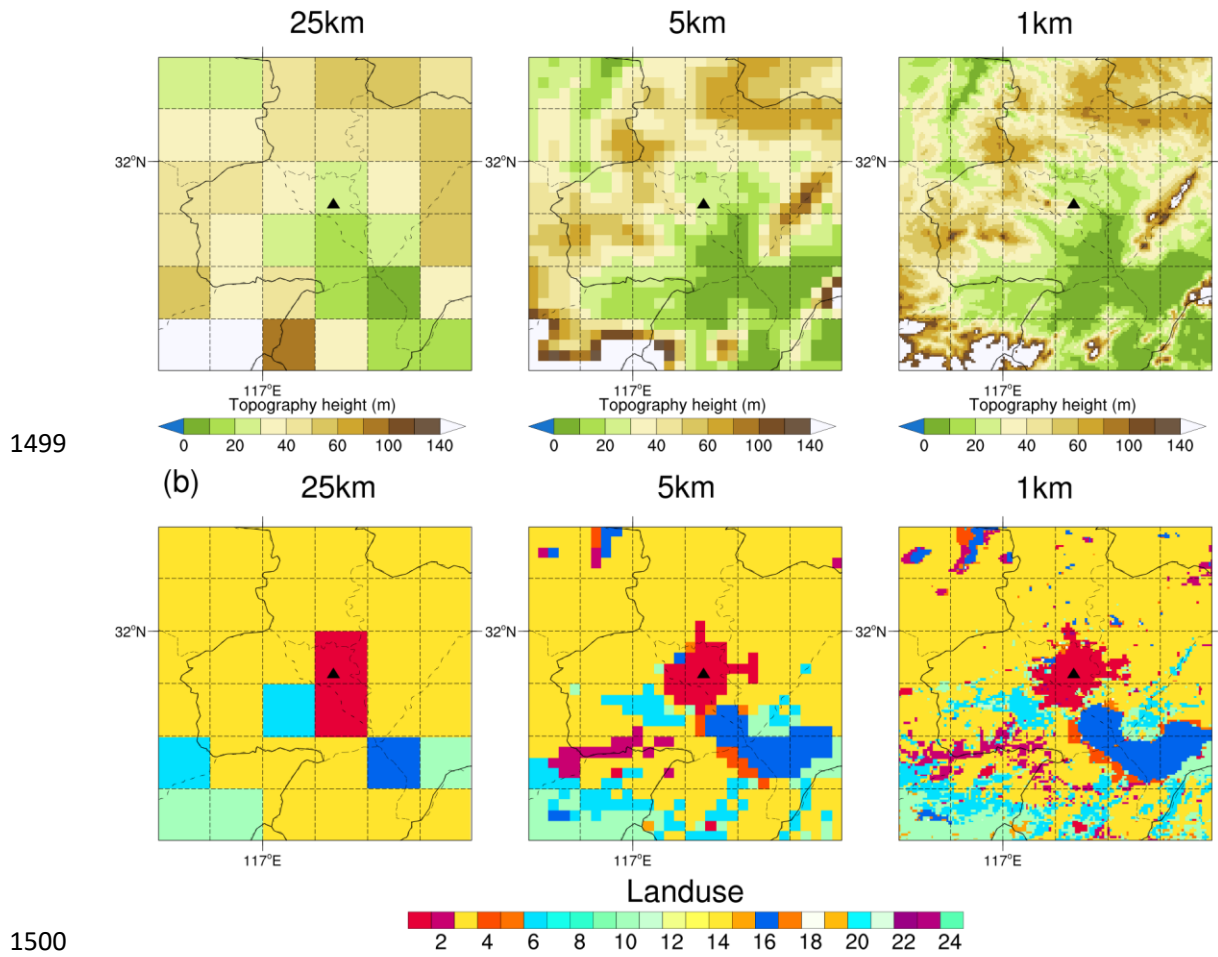
1494

1495

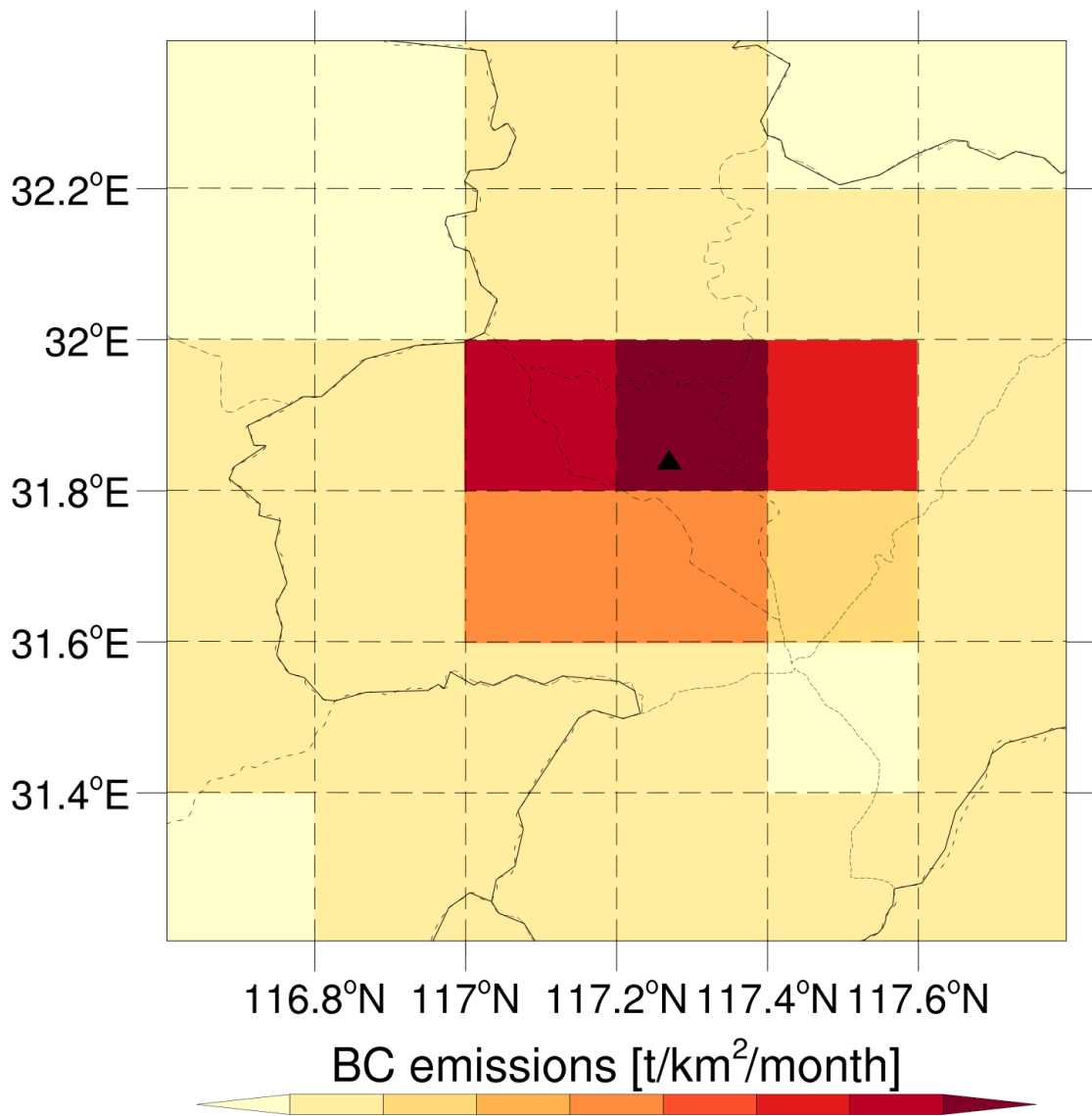
1496

1497

1498



1499 **Figure 1.** (a) The terrain height (m) in the study area for 25-km (left), 5-km (middle),
1500 and 1-km (right) resolution simulations, respectively; (b) Spatial distribution of land
1501 use types in the study area for 25-km (left), 5-km (middle), and 1-km (right) resolution
1502 simulations, respectively. The solid black triangle indicates the location of the USTC
1503 site.
1504
1505
1506
1507
1508
1509
1510
1511
1512
1513
1514



1515
1516 **Figure 2.** Spatial distribution of BC emissions in the study area. The solid black
1517 triangle indicates the location of the USTC site.

1518
1519
1520
1521
1522
1523
1524
1525
1526

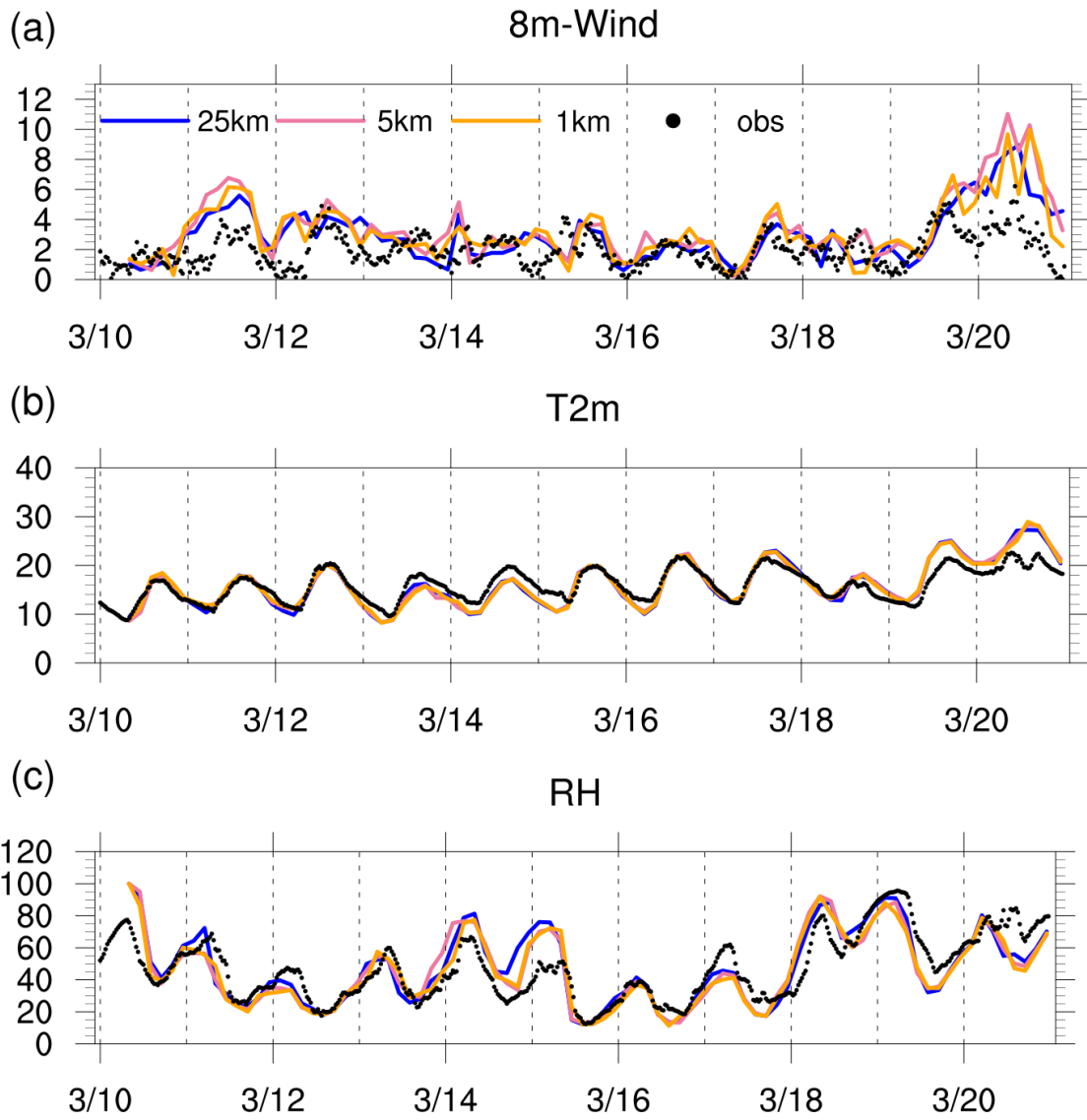


Figure 3. Time series at USTC meteorological tower observation site of observed (black dot) and simulated wind speed at 8 m (top, unit: m s^{-1}), temperature at 2 m (middle, unit: $^{\circ}\text{C}$), and relative humidity (bottom, unit: %) for 25-km (solid blue line) resolution, 5-km (solid pink line) resolution, and 1-km (solid orange line) resolution, respectively.

1533

1534

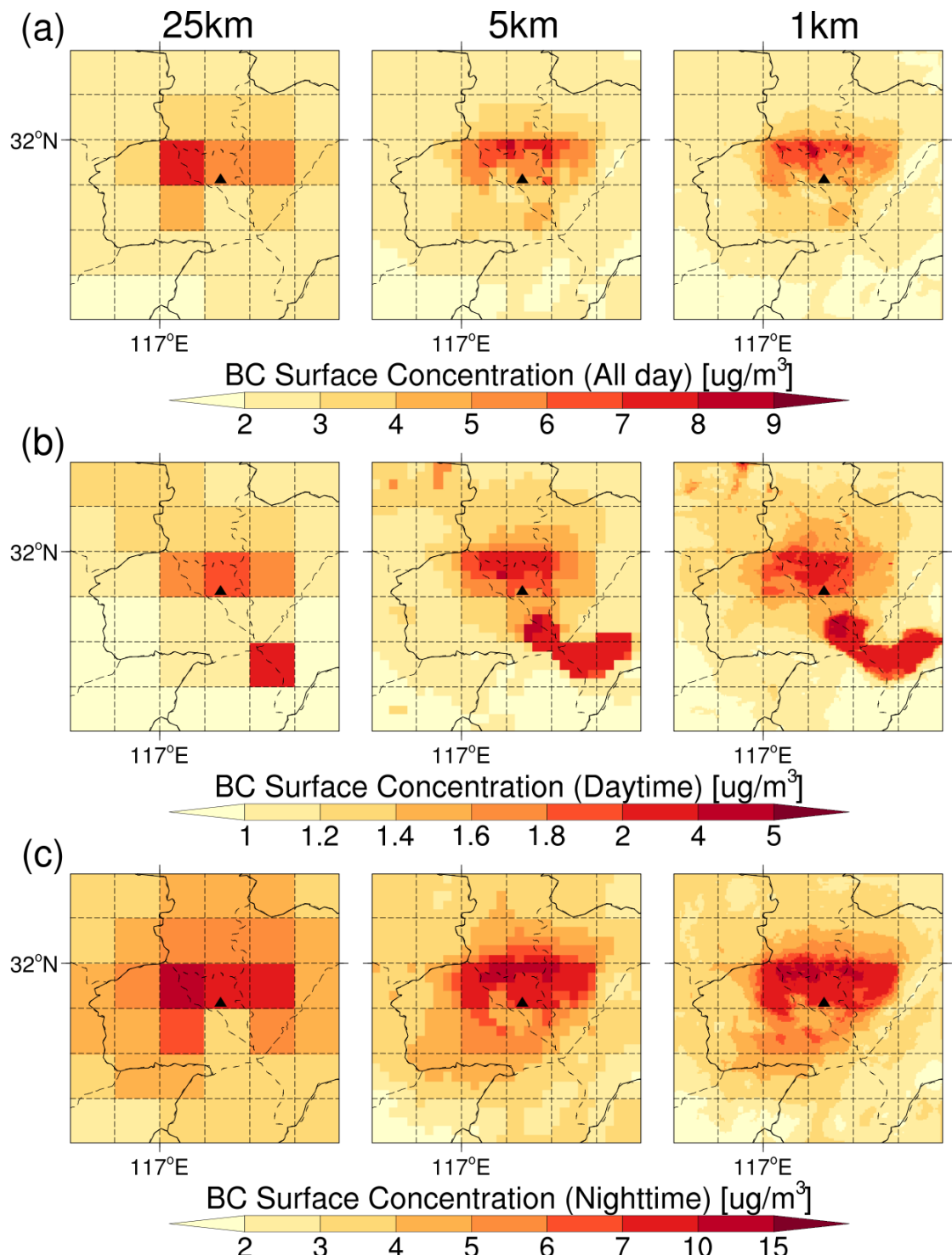
1535

1536

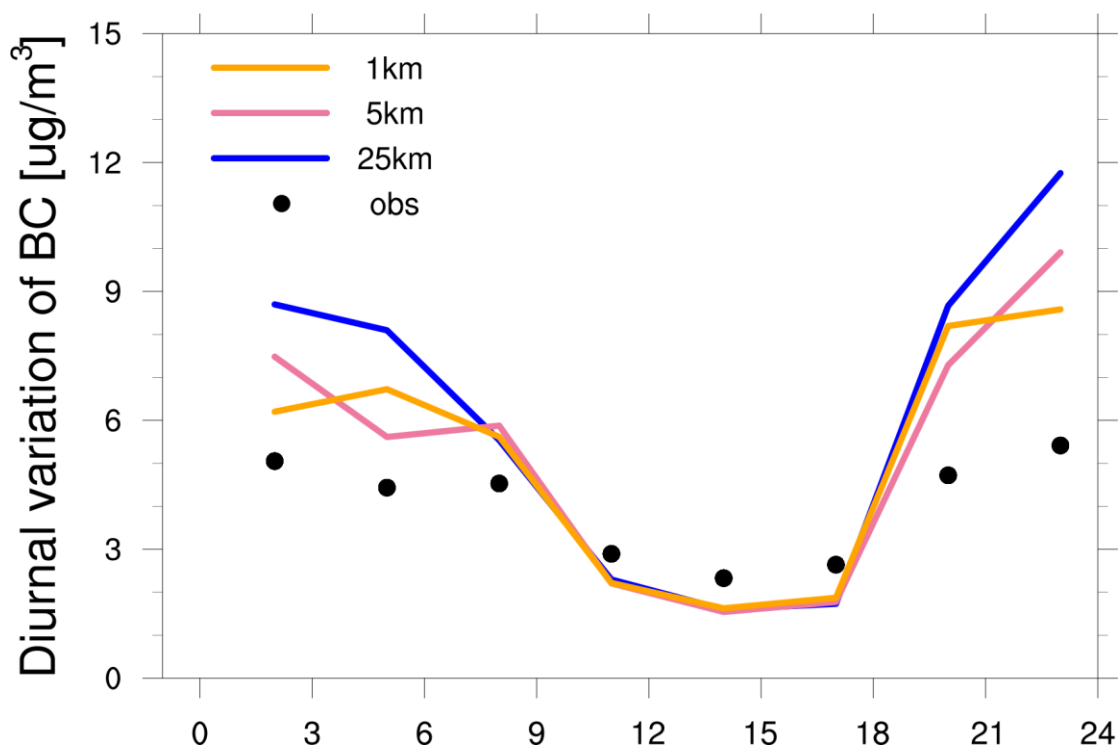
1537

1538

1539



1547



1548

1549 **Figure 5.** Diurnal variation of BC surface concentrations within 24 h averaged over
1550 the USTC site during the study period for 25-km (solid blue line), 5-km (solid pink
1551 line), and 1-km (solid orange line) resolution simulations and observations (black
1552 dot). Both the simulated results and observations are sampled at the model output
1553 frequency, i.e., 3-hourly.

1554

1555

1556

1557

1558

1559

1560

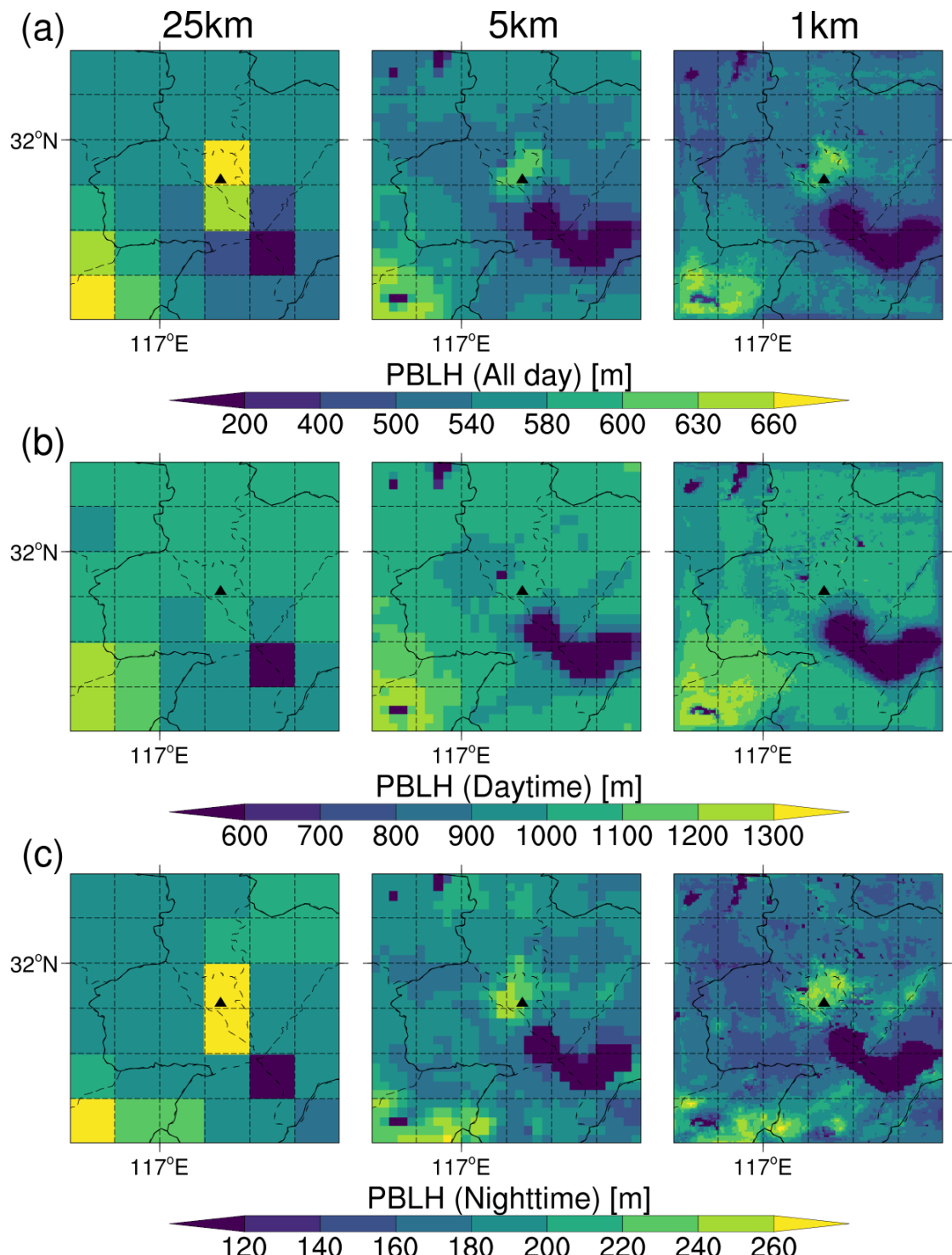
1561

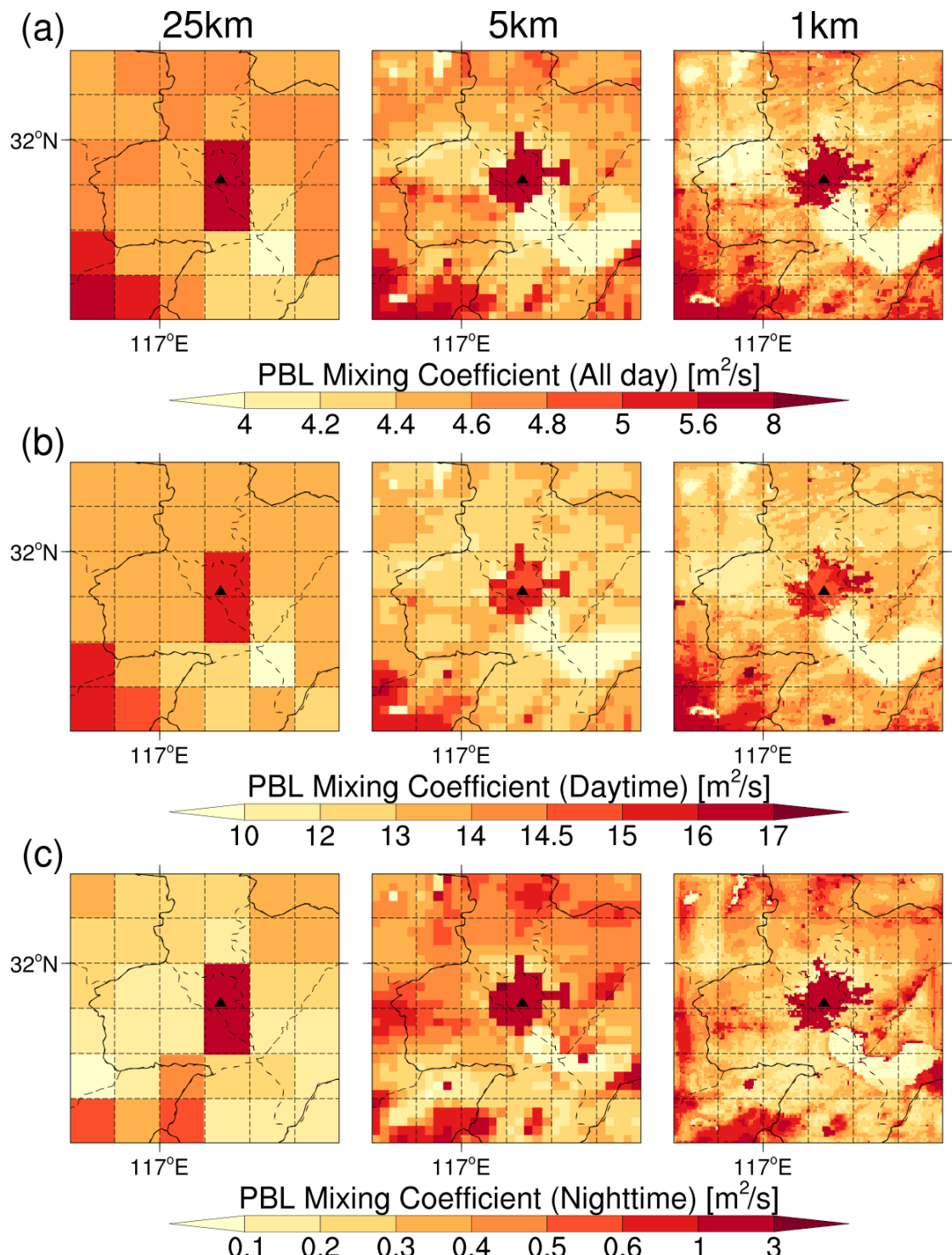
1562

1563

1564

1565

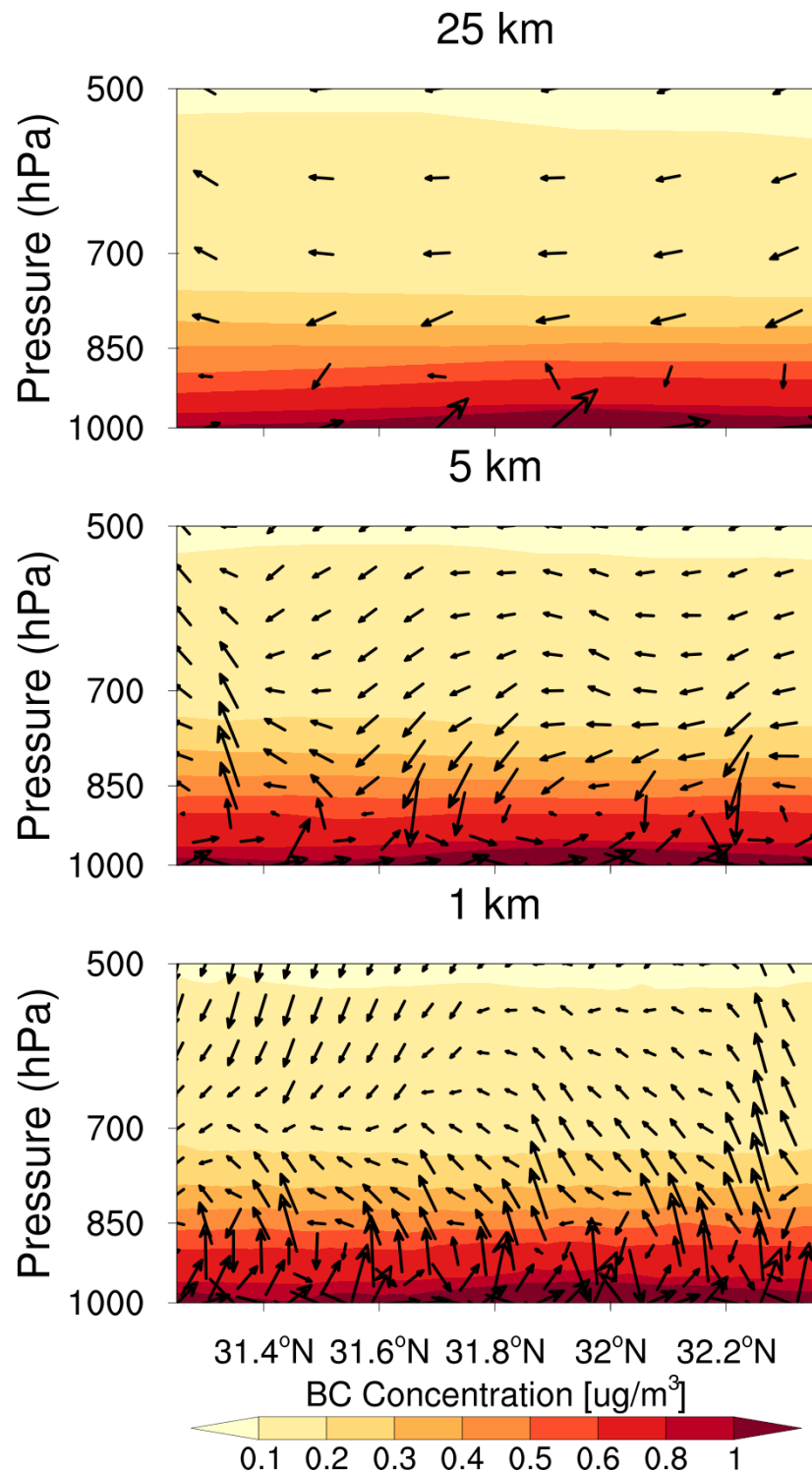




1573 **Figure 7.** Spatial distribution of PBL mixing coefficients in the study area for 25-km
 1574 (left), 5-km (middle), and 1-km (right) resolution simulations of the whole day (top),
 1575 the daytime (middle), and the nighttime (bottom), respectively. The solid black
 1576 triangle indicates the location of the USTC site.

1577

1578



1579

1580 **Figure 8.** The latitude-pressure cross section of BC concentrations and wind speed
 1581 flux along the USTC site for 25-km (top), 5-km (middle), and 1-km (bottom)
 1582 resolution simulations of the whole day, respectively. Vector arrows are the
 1583 combination of wind speed fluxes v and w , with the vertical wind speed flux being
 1584 multiplied by 100 for visibility. The shaded contours represent BC concentrations at
 1585 each pressure level.

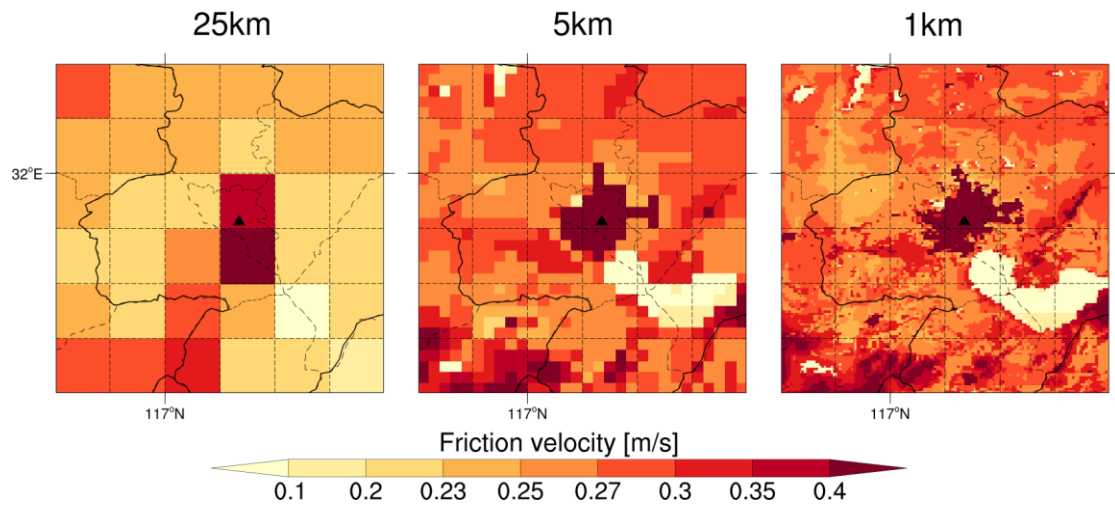


Figure 9. Spatial distribution of friction velocity in the study area for 25-km (left), 5-

km (middle), and 1-km (right) resolution simulations of the whole day, respectively.

The solid black triangle indicates the location of the USTC site.

1590

1591

1592

1593

1594

1595

1596

1597

1598

1599

1600

1601

1602

1603

1604

1605

1606

1607

1608

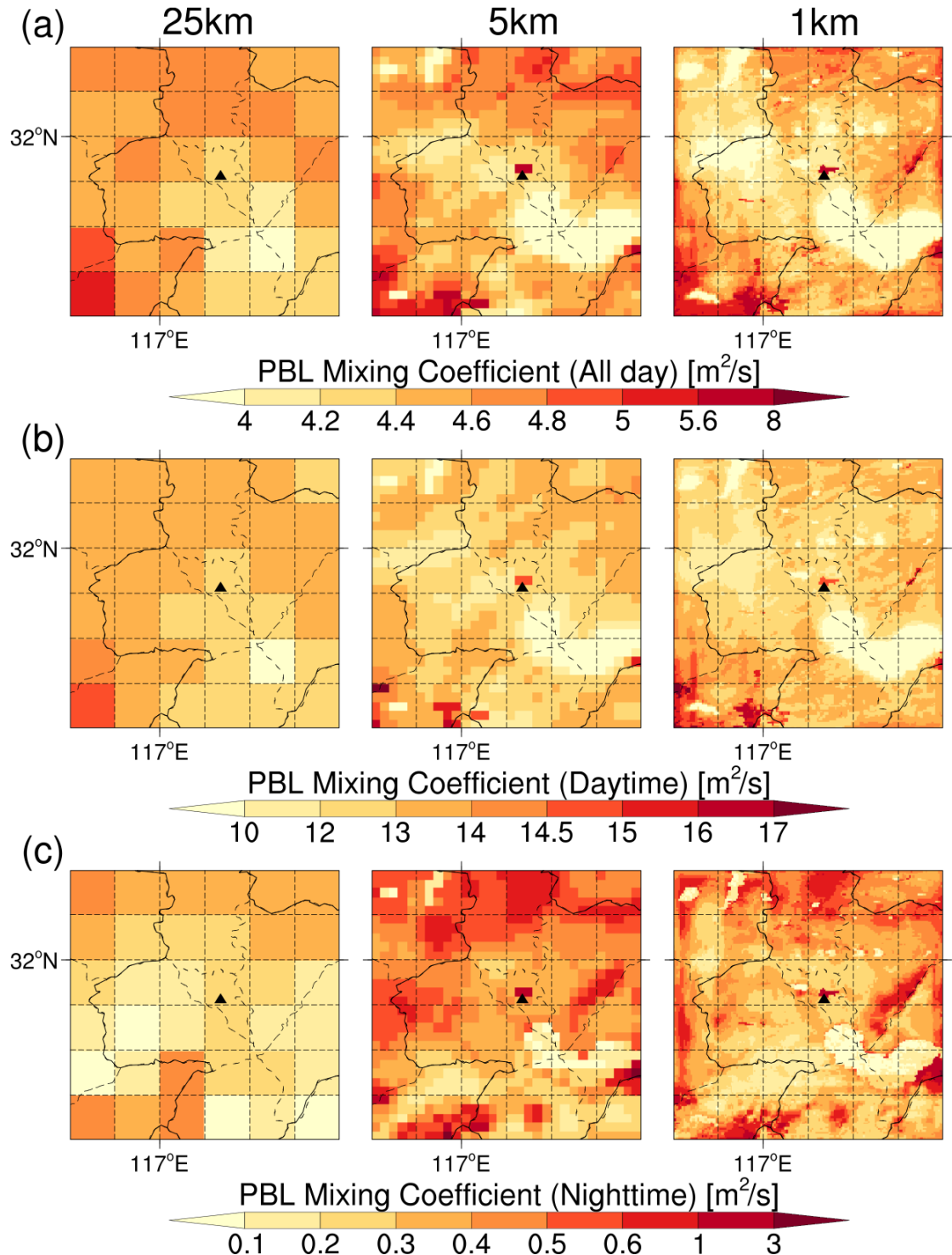
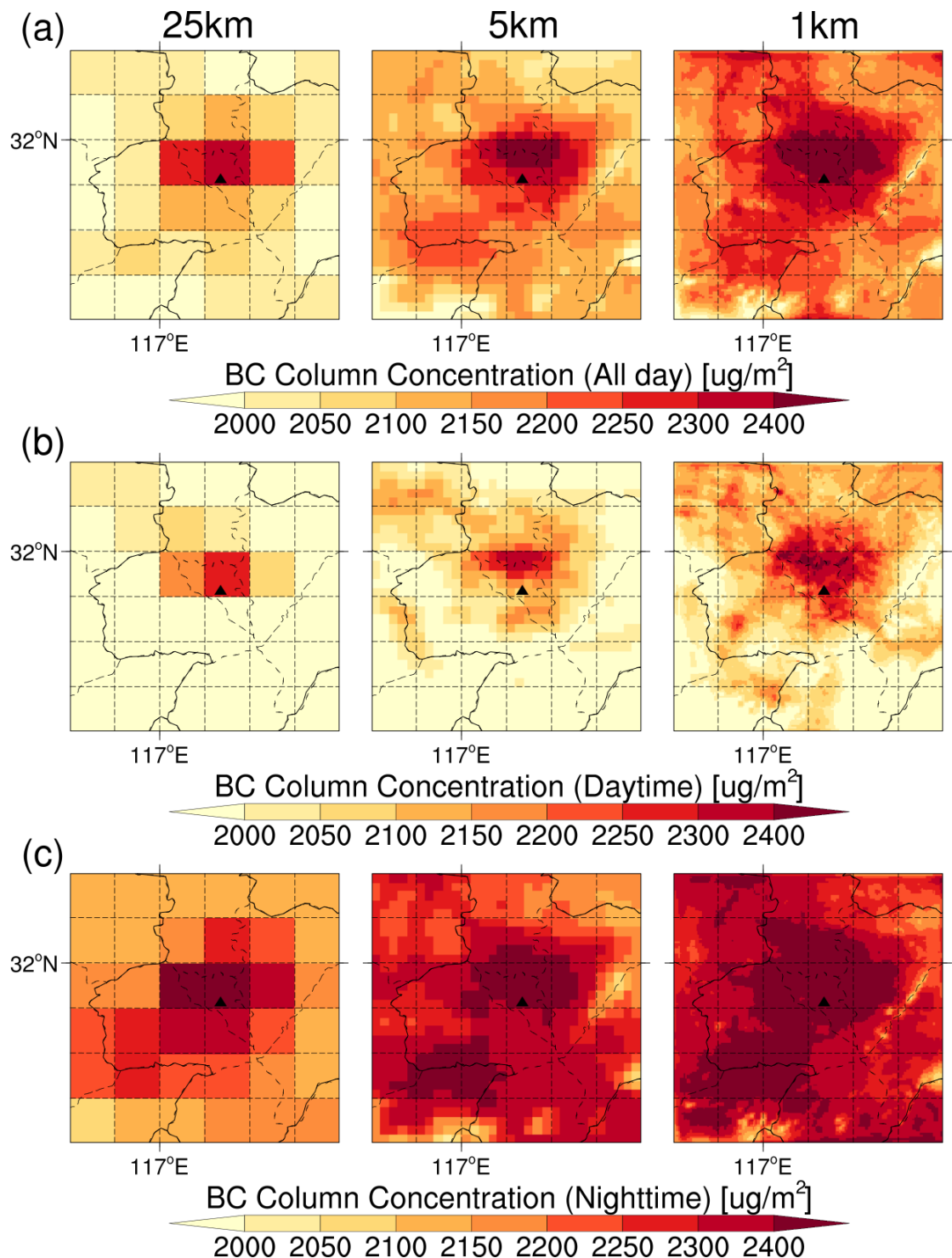


Figure 10. Spatial distribution of PBL mixing coefficients in the study area for 25-km (left), 5-km (middle), and 1-km (right) resolution simulations of the whole day (top), the daytime (middle), and the nighttime (bottom), respectively. The solid black triangle indicates the location of the USTC site. The simulation results are from the three sensitivity experiments.



1616 **Figure 11.** Spatial distribution of the BC column concentration in the study area for
1617 25-km (left), 5-km (middle), and 1-km (right) resolution simulations of the whole day
1618 (top), the daytime (middle), and the nighttime (bottom), respectively. The solid black
1619 triangle indicates the location of the USTC site.
1620

1621

1622

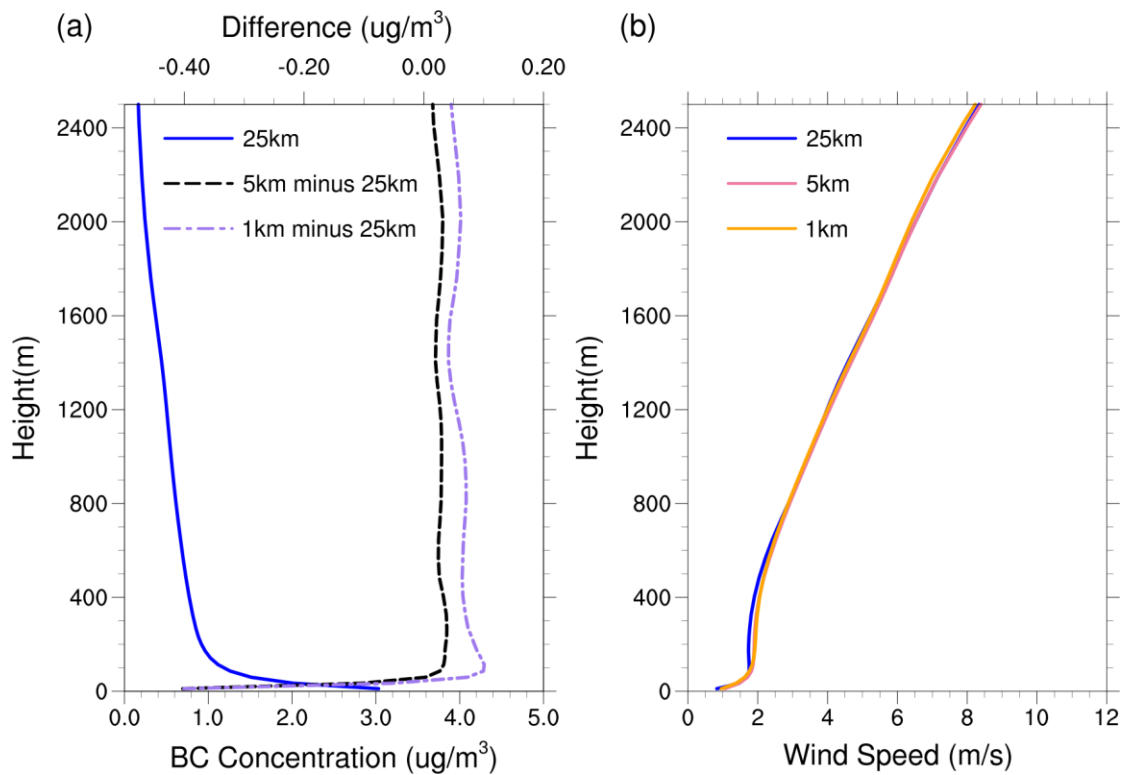


Figure 12. (a) Vertical profiles of BC concentrations simulated at 25-km resolution (solid blue line), the difference between 5-km and 25-km resolutions (dashed black line), and the difference between 1-km and 25-km resolutions (dashed purple line) averaged over the study area for the whole day, respectively. (b) Vertical profiles of wind speed simulated at 25-km resolution (solid blue line), 5-km resolution (solid pink line), and 1-km resolution (solid orange line) averaged over the study area for the whole day, respectively.

1623

1624

1625

1626

1627

1628

1629

1630

1631

1632

1633

1634

1635

1636

1637

1638

1639

1640

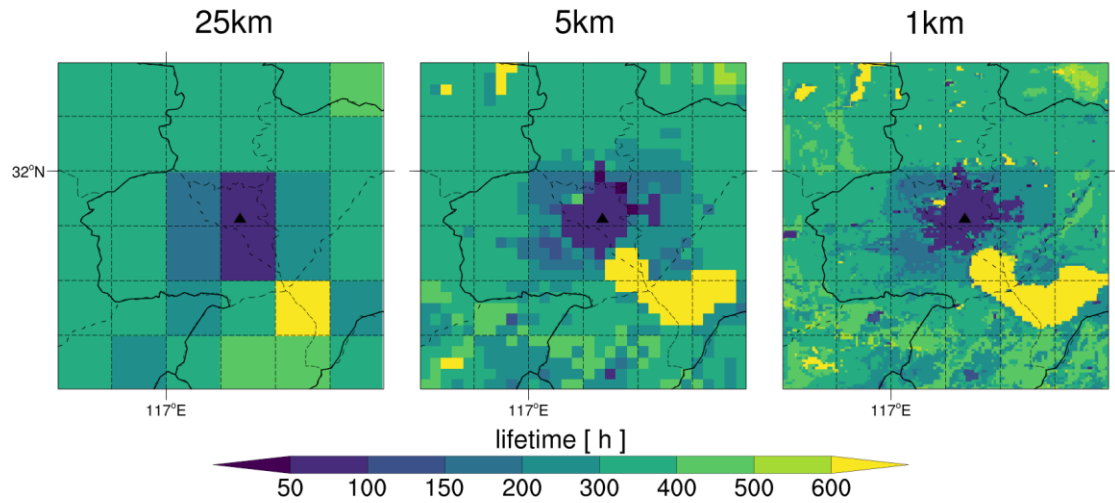


Figure 13. Spatial distribution of the lifetime in the study area for 25-km (left), 5-km (middle), and 1-km (right) resolution simulations of the whole day, respectively. The solid black triangle indicates the location of the USTC site.

1641

1642

1643

1644

1645

1646

1647

1648

1649

1650

1651